cAMP binding to closed pacemaker ion channels is non-cooperative

https://doi.org/10.1038/s41586-021-03686-x

Received: 20 October 2020

Accepted: 2 June 2021

Published online: 30 June 2021



Check for updates

David S. White^{1,2,4,7}, Sandipan Chowdhury^{1,5,7}, Vinay Idikuda^{1,6}, Ruohan Zhang^{1,2}, Scott T. Retterer³. Randall H. Goldsmith^{2™} & Baron Chanda^{1,6™}

Electrical activity in the brain and heart depends on rhythmic generation of action potentials by pacemaker ion channels (HCN) whose activity is regulated by cAMP binding¹. Previous work has uncovered evidence for both positive and negative cooperativity in cAMP binding^{2,3}, but such bulk measurements suffer from limited parameter resolution. Efforts to eliminate this ambiguity using single-molecule techniques have been hampered by the inability to directly monitor binding of individual ligand molecules to membrane receptors at physiological concentrations. Here we overcome these challenges using nanophotonic zero-mode waveguides⁴ to directly resolve binding dynamics of individual ligands to multimeric HCN1 and HCN2 ion channels. We show that cAMP binds independently to all four subunits when the pore is closed, despite a subsequent conformational isomerization to a flip state at each site. The different dynamics in binding and isomerization are likely to underlie physiologically distinct responses of each isoform to cAMP⁵ and provide direct validation of the ligand-induced flip-state model⁶⁻⁹. This approach for observing stepwise binding in multimeric proteins at physiologically relevant concentrations can directly probe binding allostery at single-molecule resolution in other intact membrane proteins and receptors.

Ligand binding to allosteric sites of transmembrane receptors such as ion channels and G-protein-coupled receptors underpins many signalling pathways. The hyperpolarization-activated, cyclic-nucleotide gated HCN ion channels are one receptor class that contributes to re-initiation of action potentials, a mechanism critical for cardiac pacemaking and rhythmic neuronal activity^{1,10}. During the 'fight or flight' response¹¹, cAMP binding to HCN modulates its activity and thereby regulates heart rate. Each HCN channel, which is a tetramer, can bind up to four cAMP molecules via its cyclic-nucleotide-binding domains (CNBDs) but the mechanism of binding and modulation remains controversial. The Hill coefficient for HCN2 exceeds unity and the channel activity reaches its maximum at 60% ligand occupancy, suggesting cooperative gating¹². Ligand-binding studies using patch clamp fluorometry (PCF) and isothermal titration calorimetry have led to unusual and complex models positing both positive and negative cooperativity, depending on the ligation state^{2,3,13}. As with any multi-parameter binding schemes based on ensemble data, these models suffer from the problem of parameter identifiability¹⁴.

The definitive approach for obtaining binding kinetics and equilibria of each ligation state is to directly monitor ligand binding at the single-molecule level. Specifically, direct resolution of ligand binding is needed to track reaction pathways, as ligand occupancy is the principal reaction coordinate for binding and gating transitions¹⁵⁻¹⁸. Intramolecular single-molecule Förster resonance energy transfer (smFRET) is a powerful technique for quantifying ligand-induced structural dyamics¹⁹⁻²⁴. However, direct measurement of cooperative ligand binding in multimeric proteins at the single-molecule level^{25,26}, including dynamics, remains an immense challenge. One key part of this challenge is performing physiologically relevant measurements above the concentration barrier of diffraction-limited light, where signal decays precipitously relative to background²⁷. Even intermolecular smFRET, which can resolve single fluorescent ligands at nanomolar concentrations in the low hundreds^{28,29}, has not been demonstrated at the micromolar concentrations required for most ion channel modulators such as cAMP³⁰. Overcoming this concentration barrier is critical for understanding the mechanism of ligand gating in multimeric ion channels and receptors.

Nanophotonic zero-mode waveguides (ZMWs) offer unique access to high concentrations⁴. ZMWs possess sub-diffraction-limit observation volumes that can resolve single binding events at micromolar³¹⁻³⁴ and even millimolar³⁵ concentrations. ZMWs facilitate long observations times needed to adequately sample ligand binding to each multimer subunit and provide the high signal to background needed to discern stacked binding events with increasing shot noise³⁶.

In this Article, we reveal the mechanism of cAMP association with purified HCN1 and HCN2 channels at the single-molecule level by using ZMWs to monitor binding of a fluorescent cAMP (fcAMP) and quantifying the transient occupation of all intermediate bound states (fully

Department of Neuroscience, University of Wisconsin-Madison, Madison, WI, USA. 2Department of Chemistry, University of Wisconsin-Madison, Madison, WI, USA. 3Center for Nanophase Materials Sciences, Oak Ridge National Laboratory, Oak Ridge, TN, USA. 4Present address: Department of Biochemistry, University of Wisconsin-Madison, Madison, WI, USA. ⁵Present address: Department of Molecular Physiology and Biophysics, University of Iowa Carver College of Medicine, Iowa City, IA, USA, ⁶Present address: Center for Investigation of Membrane Excitability Diseases, Department of Anesthesiology, Washington University School of Medicine, St Louis, MO, USA. 7 These authors contributed equally: David S. White, Sandipan Chowdhury. [™]e-mail: rhg@chem.wisc.edu; bchanda@wustl.edu

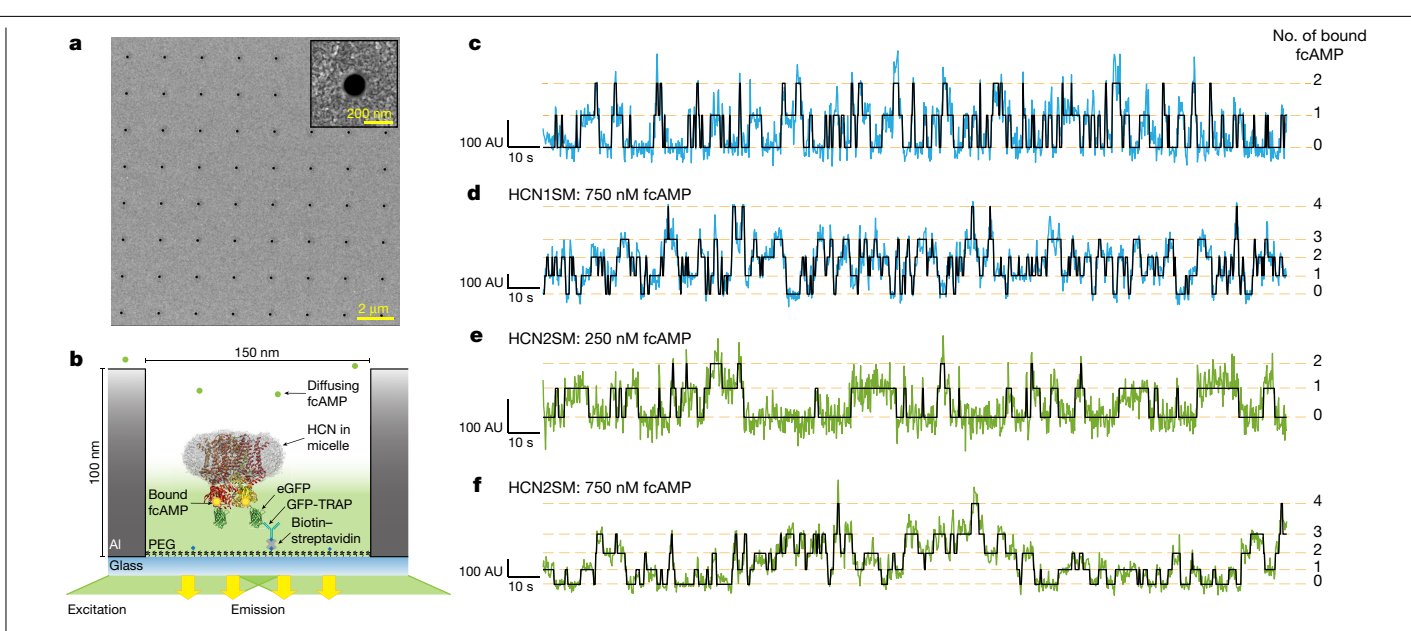


Fig. 1 | fcAMP binding to intact HCN channels in ZMWs. a, Representative scanning electron microscopy (SEM) image of ZMWs. All ZMW chips used (n=7) were confirmed by SEM. **b**, Cartoon (not to scale) of ZMW with deposited eGFP-tagged HCN for fcAMP binding experiments (eGFP, Protein Data Bank (PDB) 2YOG; HCN1, PDB 6UQG). c-f, Representative fluorescence-time

trajectories of fcAMP binding to HCN1SM and HCN2SM at 250 nM (c, e) and 750 nM (**d**, **f**) fcAMP overlaid with idealized fit (black) (120 s of 300-s trajectories are shown). Additional trajectories are presented Extended Data Figs. 3, 4.

unbound to fully bound). We find that fcAMP binding is independent for both isoforms when the pore is closed, and that each subunit independently isomerizes into a longer-lived bound conformation. We observe differences in isomerization kinetics between the two isoforms that may underlie the physiologically distinct effects of cAMP on their activation. Overall, our approach provides a detailed view of early binding transitions in a multimeric ion channel and can be applied broadly to unambiguously quantify binding cooperativity in other membrane receptors.

Binding of individual ligands to HCN channels

Full-length HCN1 and HCN2 channels were engineered with an N-terminal eGFP on each subunit for purification and imaging (HCN1SM and HCN2SM, respectively) (Methods), Electrophysiological characterization revealed activation upon hyperpolarization and modulation by cAMP, consistent with wild-type channels³⁷, including a minor shift in midpoint voltage $(V_{1/2})$ of activation for HCN1SM (+2.1 mV) and a larger shift for HCN2SM (+20.6 mV) under saturating cAMP (Extended Data Fig. 1a, b). Both channels were purified from HEK 293T cells into detergent micelles using affinity and size-exclusion chromatography (Methods, Extended Data Fig. 1c). Single-molecule photobleaching analysis confirmed the tetrameric assembly of each purified isoform under imaging conditions (Methods, Extended Data Fig. 1d).

HCN molecules were sparsely deposited into ZMWs, which were fabricated via electron-beam lithography^{4,38} (Fig. 1a, Extended Data Fig. 2, Methods), to promote single occupancy (Fig. 1b). Binding activity at various concentrations of DY-547-labelled cAMP (fcAMP) (Fig. 1c-f, Extended Data Figs. 3, 4, Supplementary Table 1) was monitored for at least 300 s at 10 Hz. Transitions between unbound (U) or multiply bound (B1, B2, B3 and B4) states were determined separately for each molecule using DISC³⁶, an unsupervised learning algorithm (Fig. 1c-f, Extended Data Figs. 3, 4, Methods).

fcAMP binds non-cooperatively to HCN isoforms

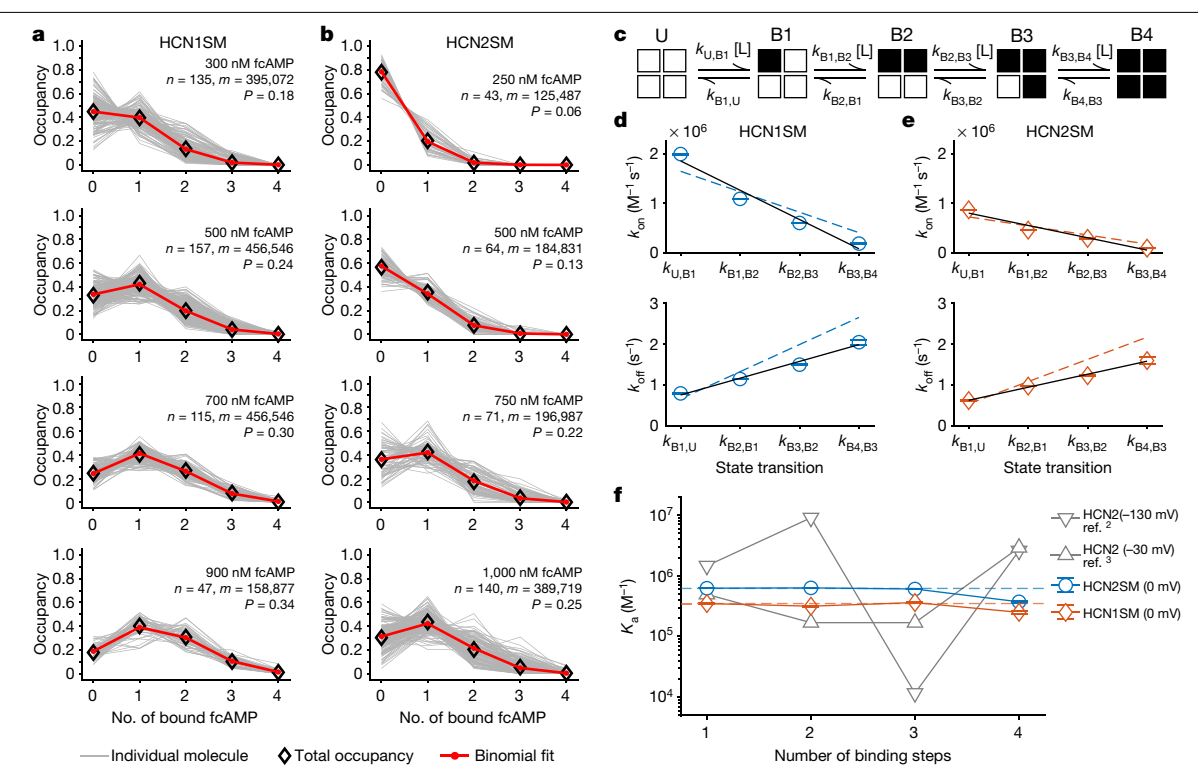
First, we determined whether the cAMP binding promotes cooperativity between different subunits. If binding to each subunit is non-cooperative, the occupancy of each ligation state obtained from idealized trajectories should follow a binomial distribution³⁹. Across all recordings, binomial fits accounted for 94% of observed state-occupancy distribution of HCN1SM and 93% for HCN2SM, as measured by root mean squared error, suggesting independent binding (Fig. 2a, b, Supplementary Table 2, Methods).

Next, we extracted transition rates by first optimizing an unconstrained sequential model with four binding transitions (Fig. 2c; model 1 in Supplementary Table 4) and the rates displayed a strong linear correlation between successive steps consistent with independent binding (Fig. 2d, e). A simpler model in which binding of individual ligands is equal, independent and governed by common rate constants³⁹ (Fig. 2d, e, dashed lines; model 2 in Supplementary Table 4) converges to similar rates as the unconstrained model. Minor deviations between these models probably arise from fewer observations of B3 and B4, our finite collection rate (10 Hz), and decreased signal-to-noise at higher fcAMP concentrations, all of which can obscure fast transitions (Supplementary Fig. 2). Equilibrium association constants (K_a) for each binding step also support non-cooperativity for both isoforms, in stark contrast to results from PCF reported elsewhere^{2,3} (Fig. 2f). The slight weak negative cooperativity between B3 and B4 arises from increased probability of missing B4 transitions and could be reproduced in simulations (Supplementary Fig. 2).

Together, state occupancies and transition rates unambiguously demonstrate that fcAMP binds non-cooperatively to intact HCN1SM and HCN2SM when the pore is closed and the voltage sensor is in the resting conformation. Our findings are in stark contrast to the oscillating behaviour from models fit from PCF data for HCN2 with the voltage sensor in either the activated or resting state^{3,12} and the negative cooperativity observed in isothermal titration calorimetry studies of isolated CNBDs¹³.

Ligand binding is followed by conformation flip

Our previous single-molecule studies on isolated HCN2 CNBDs revealed a second reversible conformational state following ligand binding^{32,35}. Combined with structural data, we postulated that this



 $Fig.\,2\,|\,fc AMP\,binds\,non-cooperatively\,to\,both\,HCN\,isoforms.$

 ${\bf a}$, ${\bf b}$, Normalized state-occupancy distributions for HCNISM (${\bf a}$) and HCN2SM (${\bf b}$) at various fcAMP concentrations with total number of molecules (n), data points (m) and binomial success rate for four subunits (P) indicated (Extended Data Fig. 5, Supplementary Table 2). ${\bf c}$, Sequential ligand-binding model (model 1 in Supplementary Table 4). White squares indicate unbound (U), black squares indicate bound (B) and L represents ligand. ${\bf d}$, ${\bf e}$, Optimized transition rates (mean \pm s.e.m.) for sequential binding (Supplementary Table 5) for HCNISM (${\bf d}$)

and HCN2SM (**e**) with a linear fit (black solid). Dashed lines indicate expected rates from constrained and sequential non-cooperative binding model (model 2 in Supplementary Table 4). **f**, Equilibrium association constants (K_a) for each ligand-binding step (mean \pm s.e.m.). Dashed lines indicate fits from model 2. Previously reported K_a values for fcAMP binding to HCN2 using PCF of open² (–130 mV) and closed³ (–30 mV) channels shown for comparison (grey). For **d**-**f**, parameters were fit to all events across all fcAMP concentrations (HCN1SM: 739 molecules, 180,480 events; HCN2SM: 444 molecules, 82,030 events).

second conformation corresponds to a coordinated rotation of the N- and C-terminal α -helices about the rigid CNBD β -barrel 32 , reminiscent of a catch-and-hold mechanism of ligand-gated channels $^{6-9}$. A similar model of ligand docking and CNBD isomerization was suggested by double electron–electron resonance (DEER) spectroscopy 40 . It has previously been hypothesized that this ligand-induced 'flipped' state may allosterically modulate the pore through the C-linker 40,41 . Whether these conformational dynamics observed in isolated CNBDs are preserved in full-length channels remained an open question.

We first analysed dwell times of singly-liganded states immediately preceded and followed by unbound states $(U \!\!\rightarrow\!\! B1 \!\!\rightarrow\!\! U)$ as these dwell times provide the most accurate representation of individual binding dynamics without truncation from additional binding (Fig. 3a). Maximum-likelihood estimations of isolated-B1 dwell time distributions required two exponential components for both HCN1SM and HCN2SM (Fig. 3b, c), with the monoexponential fit conspicuously failing, particularly for HCN2SM, at both early and late times (Extended Data Figs. 6, 7, Supplementary Table 3). The contribution of static disorder to the histogram can also be ruled out (Extended Data Fig. 8). These analyses suggest an isomerization into a flipped state at each subunit following ligand binding in intact HCN channels. Critically, as binding is non-cooperative, this conformational change does not influence ligand association with neighbouring subunits when the channel is closed.

Binding dynamics underlie ligand efficacy

The existence of the ligand-induced flipped state across all CNBDs was assessed by testing two models featuring four independent binding steps either without (model 2 in Supplementary Table 4) or with ligand

induced isomerization upon binding (Fig. 4a, model 3 in Supplementary Table 4). Both models were validated using representative simulations to ensure reliability (Supplementary Figs. 1, 2, Supplementary Methods).

Transition rates were globally optimized using QuB and ranked by Bayesian information criterion to optimize goodness of fit and model complexity⁴²⁻⁴⁴ (Methods). Consistent with studies on isolated monomeric CNBDs^{32,35} and the isolated-B1 dwell times above, the model featuring a conformational flip at each subunit was preferred for both HCN1SM and HCN2SM (Supplementary Table 4). Therefore, the null hypothesis of purely sequential binding can be rejected in favour of a scheme featuring reversible conformational flips of ligand-occupied subunits.

Optimized transition rates from model 3 provide insights into mechanistic differences between HCN isoforms (Fig. 4b). Simulations of optimized rates for each isoform match experimentally observed fractional occupancy (Fig. 4c) and dwell time distributions of each liganded state (Extended Data Figs. 9,10). HCNISM and HCN2SM exhibit similar unbinding rates, but the ligand-association rate of HCN1SM is nearly twice as fast. Each isoform exhibits similar rates of exiting the flipped state, but HCN1SM spends only 27% of the time in the flipped state for any bound event, compared to 43% for HCN2SM owing to its faster entry rate. These results suggest that differences in cAMP modulation ability of HCN channels derive not only from differences in ligand association, but also from the duration of time spent in a second metastable conformation.

Discussion

Here, we directly quantified the transient occupation of each of the four ligation states of two functionally distinct HCN isoforms at the

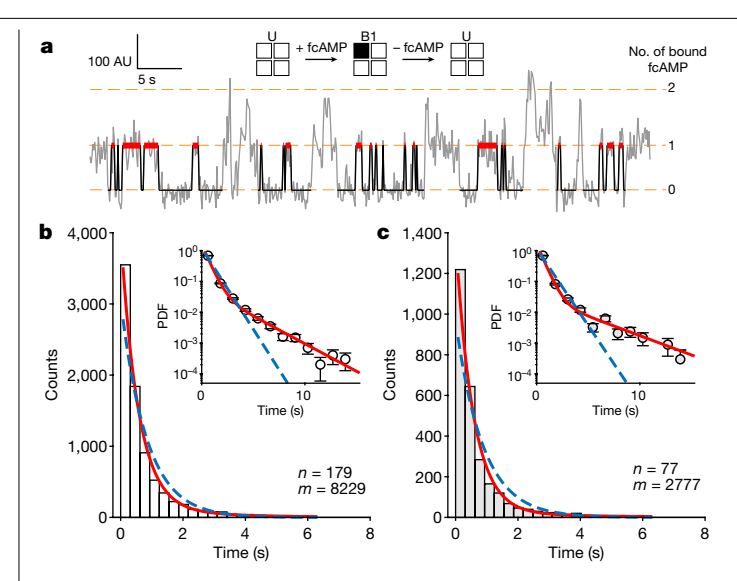


Fig. 3 | Ligand binding induces a conformational change at each HCN subunit. a, Representative fcAMP binding trajectory with identified isolated-B1 dwell times (red). b, c, Dwell time distributions of isolated-B1 events for HCN1SM (b) and HCN2SM (c) at 250 nM fcAMP overlaid with monoexponential (blue dashed) and biexponential (red) fits (Methods). n is the total number of molecules and m is the total number of dwell times. Abscissa values correspond to the centre of the histogram bars. Insets show probability density function (PDF) of each distribution with the ordinate on a log scale to highlight less-frequent but long-lived bound durations. Error bars show the error of binomial distribution for each bin. See Extended Data Figs. 6, 7 for isolated-B1 dwell time distributions and Supplementary Table 3 for all fit parameters.

single-molecule level using ZMWs. Our approach overcomes the current limitations of ensemble measurements and offers several key insights into the mechanism of ligand activation. First, we find that the binding of each of the four fcAMPs to functional HCN1SM or HCN2SM channels occurs independently when the channel pore is closed in absence of membrane potential. Although previous observations that isolated CNBDs oligomerize upon cAMP binding suggested cooperativity^{41,45}, there is no evidence that this association also occurs in intact channels. Indeed, single-particle reconstructions of HCN channels do not show any evidence of cAMP-induced association between CNBDs⁴⁶. However, we cannot rule out the possibility that ligand binding is cooperative if the membrane is sufficiently hyperpolarized to open HCN channels.

Second, we resolved a second, metastable conformational state following ligand binding at each subunit. Using single-channel analysis on glycine receptors, Sivilotti and colleagues postulated that ligand binding is followed by a global and coordinated conformational rearrangement to stabilize binding⁶⁻⁹. In contrast to the single unique conformation predicted from these models, our data instead show that the flip state is an ensemble of conformations with independent conformational changes at each subunit. Our revised flip-state model closely matches structural data from isolated CNBDs^{32,40} and full-length channels⁴⁶. Whether these previously identified structural transitions correspond to the kinetic intermediates observed here remains to be determined.

Finally, we uncover subtle but important differences in the dynamics between the two isoforms. Despite similar fcAMP unbinding rates, HCN2SM subunits enter the flip state faster, leading to increased bound durations. This suggests that prolonged duration in the stabilizing flip conformation may underlie the stronger effect of cAMP on pore modulation in HCN2 than HCN1. Our data therefore contradict the notion that HCN1 channels exists primarily in a high-affinity conformation (pre-activated state model) leading to unresponsiveness to cAMP binding45.

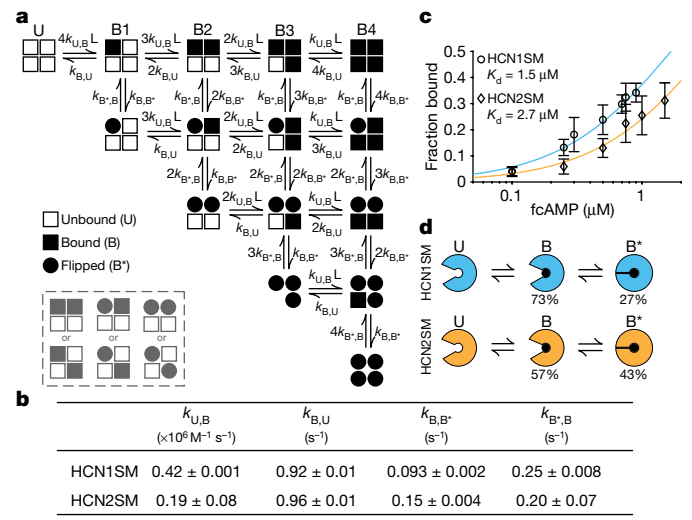


Fig. 4 | A revised flip-state model. a, Non-cooperative binding model with a reversible conformational flip at each subunit following binding of ligand (L). Alternative binding patterns are outlined in the dashed box. b, Optimized transitions rates of binding states shown in a for HCN1SM and HCN2SM. Data $are\,mean\,\pm\,s.e.m.\,\boldsymbol{c}, Binding\,curve\,of\,HCN1SM\,and\,HCN2SM\,at\,various\,fcAMP$ concentrations overlaid with predictions from a (mean ± s.d.). Numbers of molecules for each fcAMP concentration are provided in Supplementary Table 1. d, Schematic showing conversion efficiency between unbound (U), bound (B) and flipped (B*) states for HCN1SM and HCN2SM.

Overall, we have developed an approach to dynamically monitor the binding of multiple individual ligands to a membrane receptor at single-molecule resolution, offering a paradigm for studying $ligand-dependent \, activation \, in \, many \, multimeric \, ligand-gated \, ion \, chandra \, chandr$ nels and receptors (Supplementary Note 1). These measurements can quantify ligand-induced gating processes and can potentially be combined with smFRET to identify key structural transitions. Our approach can be used more widely to study the effect of allosteric modulators and drugs, including agonists, antagonists and partial and inverse agonists on ligand binding to clarify their mechanisms of action, bringing us closer to a comprehensive understanding of ligand-dependent activation in membrane receptors.

Online content

Any methods, additional references, Nature Research reporting summaries, source data, extended data, supplementary information, acknowledgements, peer review information; details of author contributions and competing interests; and statements of data and code availability are available at https://doi.org/10.1038/s41586-021-03686-x.

- Wahl-Schott, C. & Biel, M. HCN channels: structure, cellular regulation and physiological function. Cell. Mol. Life Sci. 66, 470-494 (2009).
- Kusch, J. et al. How subunits cooperate in cAMP-induced activation of homotetrameric HCN2 channels, Nat. Chem. Biol. 8, 162-169 (2011).
- 3. Thon, S., Schulz, E., Kusch, J. & Benndorf, K. Conformational flip of nonactivated HCN2 channel subunits evoked by cyclic nucleotides, Biophys. J. 109, 2268-2276 (2015).
- Levene, M. J. et al. Zero-mode waveguides for single-molecule analysis at high concentrations, Science 299, 682-686 (2003).
- Wainger, B. J., DeGennaro, M., Santoro, B., Siegelbaum, S. A. & Tibbs, G. R. Molecular mechanism of cAMP modulation of HCN pacemaker channels. Nature 411. 805-810 (2001).
- Lape, R., Colquhoun, D. & Sivilotti, L. G. On the nature of partial agonism in the nicotinic receptor superfamily, Nature 454, 722-727 (2008)
- Jadey, S. & Auerbach, A. An integrated catch-and-hold mechanism activates nicotinic acetylcholine receptors. J. Gen. Physiol. 140, 17-28 (2012).
- Abele, R., Keinanen, K. & Madden, D. R. Agonist-induced isomerization in a glutamate receptor ligand-binding domain. A kinetic and mutagenetic analysis. J. Biol. Chem. 275, 21355-21363 (2000).
- Cheng, Q., Du, M., Ramanoudjame, G. & Jayaraman, V. Evolution of glutamate interactions during binding to a glutamate receptor, Nat. Chem. Biol. 1, 329-332 (2005).

- DiFrancesco, D. The role of the funny current in pacemaker activity. Circ. Res. 106, 434-446 (2010)
- DiFrancesco, D. & Tortora, P. Direct activation of cardiac pacemaker channels by intracellular cyclic AMP. Nature 351, 145-147 (1991).
- Kusch, J. et al. Interdependence of receptor activation and ligand binding in HCN2 pacemaker channels. Neuron 67, 75-85 (2010).
- Chow, S. S., Van Petegem, F. & Accili, E. A. Energetics of cyclic AMP binding to HCN channel C terminus reveal negative cooperativity. J. Biol. Chem. 287, 600-606 (2012).
- Hines, K. E., Middendorf, T. R. & Aldrich, R. W. Determination of parameter identifiability in nonlinear biophysical models: a Bayesian approach. J. Gen. Physiol. 143, 401-416 (2014).
- Wyman, J. The binding potential, a neglected linkage concept. J. Mol. Biol. 11, 631-644
- Sigg, D. A linkage analysis toolkit for studying allosteric networks in ion channels. J. Gen. 16. Physiol. 141, 29-60 (2013).
- Chowdhury, S. & Chanda, B. Free-energy relationships in ion channels activated by 17. voltage and ligand. J. Gen. Physiol. 141, 11-28 (2013).
- 18. Chowdhury, S. & Chanda, B. Estimating the voltage-dependent free energy change of ion channels using the median voltage for activation, J. Gen. Physiol, 139, 3-17 (2012).
- Vafabakhsh, R., Levitz, J. & Isacoff, E. Y. Conformational dynamics of a class C 19 G-protein-coupled receptor. Nature 524, 497-501 (2015).
- 20 Gregorio, G. G. et al. Single-molecule analysis of ligand efficacy in $\beta_2 \text{AR-G-protein}$ activation. Nature 547, 68-73 (2017).
- 21 Liauw, B. W., Afsari, H. S. & Vafabakhsh, R. Conformational rearrangement during activation of a metabotropic glutamate receptor. Nat. Chem. Biol. 17, 291-297 (2021).
- Wang, Y. et al. Single molecule FRET reveals pore size and opening mechanism of a mechano-sensitive ion channel. eLife 3, e01834 (2014).
- Dolino, D. M. et al. The structure-energy landscape of NMDA receptor gating. Nat. Chem. Biol. 13, 1232-1238 (2017).
- Wang, S., Vafabakhsh, R., Borschel, W. F., Ha, T. & Nichols, C. G. Structural dynamics of potassium-channel gating revealed by single-molecule FRET. Nat. Struct. Mol. Biol. 23,
- Jiang, Y. et al. Sensing cooperativity in ATP hydrolysis for single multisubunit enzymes in solution. Proc. Natl Acad. Sci. USA 108, 16962-16967 (2011).
- Hoskins, A. A. et al. Ordered and dynamic assembly of single spliceosomes. Science 331, 1289-1295 (2011).
- Holzmeister, P., Acuna, G. P., Grohmann, D. & Tinnefeld, P. Breaking the concentration limit of optical single-molecule detection. Chem. Soc. Rev. 43, 1014-1028 (2014).
- Wu, J. Y., Stone, M. D. & Zhuang, X. A single-molecule assay for telomerase 28. structure-function analysis. Nucleic Acids Res. 38, e16 (2010).
- Morse, J. C. et al. Elongation factor-Tu can repetitively engage aminoacyl-tRNA within the ribosome during the proofreading stage of tRNA selection. Proc. Natl Acad. Sci. USA 117, 3610-3620 (2020).

- 30. Zheng, J. & Trudeau, M. C. Handbook of Ion Channels (CRC, 2015).
- Zhu, P. & Craighead, H. G. in Annual Review of Biophysics Vol. 41 (ed. D. C. Rees) 269-293 (2012).
- Goldschen-Ohm, M. P. et al. Structure and dynamics underlying elementary ligand 32. binding events in human pacemaking channels. eLife 5, e20797 (2016).
- 33. Uemura, S. et al. Real-time tRNA transit on single translating ribosomes at codon resolution. Nature 464, 1012-1017 (2010).
- 34. Eid, J. et al. Real-time DNA sequencing from single polymerase molecules. Science 323, 133-138 (2009).
- Goldschen-Ohm, M. P., White, D. S., Klenchin, V. A., Chanda, B. & Goldsmith, R. H. Observing single-molecule dynamics at millimolar concentrations. Angew. Chem. Int. Ed. **56**, 2399-2402 (2017).
- White, D. S., Goldschen-Ohm, M. P., Goldsmith, R. H. & Chanda, B. Top-down machine learning approach for high-throughput single-molecule analysis. eLife 9, e53357 (2020).
- Wang, J., Chen, S. & Siegelbaum, S. A. Regulation of hyperpolarization-activated HCN channel gating and cAMP modulation due to interactions of COOH terminus and core transmembrane regions, J. Gen. Physiol. 118, 237-250 (2001).
- 38. Korlach, J. et al. Selective aluminum passivation for targeted immobilization of single DNA polymerase molecules in zero-mode waveguide nanostructures. Proc. Natl Acad. Sci. USA 105, 1176-1181 (2008).
- Ding, S. & Sachs, F. Evidence for non-independent gating of P2X₂ receptors expressed in Xenopus oocytes. BMC Neurosci. 3, 17 (2002).
- Collauto, A. et al. Rates and equilibrium constants of the ligand-induced conformational transition of an HCN ion channel protein domain determined by DEER spectroscopy Phys. Chem. Chem. Phys. 19, 15324-15334 (2017).
- Zagotta, W. N. et al. Structural basis for modulation and agonist specificity of HCN pacemaker channels. Nature 425, 200-205 (2003).
- Qin, F., Auerbach, A. & Sachs, F. A direct optimization approach to hidden Markov modeling for single channel kinetics. Biophys. J. 79, 1915-1927 (2000).
- Nicolai, C. & Sachs, F. Solving ion channel kinetics with the QuB software. Biophys. Rev. Lett. 8, 191-211 (2013).
- Schwarz, G. Estimating dimension of a model. Ann. Stat. 6, 461-464 (1978).
- 45. Lolicato, M. et al. Tetramerization dynamics of C-terminal domain underlies isoform-specific cAMP gating in hyperpolarization-activated cyclic nucleotide-gated channels. J. Biol. Chem. 286, 44811-44820 (2011).
- Lee, C. H. & MacKinnon, R. Structures of the human HCN1 hyperpolarization-activated channel. Cell 168, 111-120.e11 (2017).

Publisher's note Springer Nature remains neutral with regard to jurisdictional claims in published maps and institutional affiliations.

© The Author(s), under exclusive licence to Springer Nature Limited 2021

Methods

No statistical methods were used to predetermine sample size. The experiments were not randomized. The investigators were not blinded to allocation during experiments and outcome assessment.

Generation of single-molecule constructs

HCN1SM was based off a cryo-electron microscopy study of HCN1⁴⁶. We modified the human orthologue of HCN1 by deleting amino acids 636–865 on the C-terminal tail and on the N terminus the construct was tagged with eGFP and a Twin-strep affinity purification tag. The eGFP tag was used for both single-molecule localization and tethering to streptavidin-coated surfaces via a biotinylated GFP nanobody (GFP-TRAP). The mouse orthologue of HCN2 was modified to yield HCN2SM. Amino acids corresponding to residues 686–860 on the C terminus were deleted to improve the biochemical behaviour of the purified protein and the amino acids corresponding to residues 1–136 on the N terminus were replaced by residues 1–98 from the human HCN1 orthologue to overcome the high G/C content. HCN2SM, as with HCN1SM, was tagged on the N terminus with Twin Strep-tag and eGFP.

Cell culture and electrophysiology

HEK 293T adherent cells (ATCC) were cultured in DMEM (Sigma) with 10% FBS (Gibco). The HEK 293T cells were not experimentally authenticated or tested for mycoplasma contamination. For transient transfection, cells were seeded in 35-mm cell culture dishes. After 16-20 h, the cells were transiently transfected with 2.5 µg of either HCN1SM or HCN2SM plasmid DNA using TransIT-293 reagent (MIRUS) as per manufacturer's instructions. In case of HCN2SM transfected cells, 10 mM sodium butyrate was added 12 h post transfection to boost the protein expression. 48-60 h post transfection, the solution in the dish was exchanged with external solution (130 mM NaCl, 30 mM KCl, 1.8 mM CaCl₂, 5 mM HEPES, 0.5 mM MgCl₂, pH7.4; 310 mOsm). Recording electrodes (Drummond scientific, OD 1.6 mm) with a resistance of around $2-4 \,\mathrm{M}\Omega$ were pulled using P-97 puller (Sutter Instrument). Electrodes were fire polished and filled with the internal solution (130 mM KCl, 10 mM NaCl, 1 mM EGTA, 0.5mM MgCl₂ and 5 mM HEPES, 2mM ATP (ATP sodium salt), pH7.2; 295 mOsm). Where indicated, internal solution also contained 500 µM cAMP (cyclic adenosine monophosphate sodium salt). Whole-cell recordings were obtained at room temperature (23 °C) using an Axopatch 200A amplifier, a Digidata 1550B digitizer and pCLAMP software (version 10.7, Molecular Devices). Recordings were low pass filtered at 5 kHz and sampled at 20 kHz. Activation curves were obtained by holding the cell at 0 mV and then hyperpolarizing to -30 to either -130 mV (for HCN1SM) or -150 mV (for HCN2SM) in 10 mV decrements, followed by a test pulse at -130 mV. All the statistical analysis was performed using OriginPro 2020b and the data are presented as mean ± s.e.m. (Extended Data Fig. 1a, b).

Protein expression and purification

cDNA corresponding to HCNISM in the modified pEG BacMam vector was extracted from large volumes of bacterial cultures using Endotoxin free Plasmid Purification kits (Qiagen) and transfected into suspension cultures of Freestyle HEK 293 cells (Thermo Fisher Scientific) using Trans-IT Pro Transfection reagent (MIRUS) following manufacturer's instructions. The Freestyle HEK93 cells were not experimentally authenticated or tested for mycoplasma contamination. Post transfection, cells were grown at 12–14 h at 37 °C, following which sodium butyrate was added to the cultures to a final concentration of 10 mM and cultures were grown at 30 °C for another 48 h. Cells were collected by centrifugation at 3,000g for 20 min and washed twice with chilled 150 mM NaCl, 2 0mM Tris, pH 8.0. Cell pellets were subsequently resuspended in lysis buffer (300 mM NaCl, 40 mM Tris, 10 mM DTT, 20% glycerol, 1 mM EDTA, 1% L-MNG, 2 mM cholesterol hemi succinate (CHS), pH 8.0 supplemented with 1× Halt protease inhibitor cocktail (Thermo Fisher Scientific),

briefly sonicated on ice and incubated at 4 °C with gentle agitation for about 2 h. The detergent extract was spun at about 100,000g for 1.5 h and the supernatant was purified using Streptactin affinity resin (IBA Life Sciences). Protein bound resin was washed with 10 bed volumes of wash buffer (300 mM NaCl, 20 mM Tris, 10 mM DTT, 5% glycerol, 1 mM EDTA, 0.1% digitonin (Calbiochem), pH 8.0) and the protein was eluted in wash buffer with 5 mM desthiobiotin. The eluent was concentrated using 100 MWCO centrifugal filters to about 500 μ l and further purified using size exclusion chromatography (SEC) on the Superose 6 Increase column at 4 °C. The SEC Buffer used was 300 mM NaCl, 20 mM Tris, 10 mM DTT, 0.1 mM GDN, pH 8.0. All single-molecule experiments were performed with the peak fraction of the protein (which routinely contained 30-100 nM protein) within 2–6 h of the SEC step (Extended Data Fig. 1c).

HCN2SM was expressed in suspension cultures of Freestyle HEK 293 cells as described above for HCN1SM. Purification of HCN2SM was modified from that of HCN1SM in the following ways. The lysis buffer used 1% digitonin (instead of L-MNG/CHS) and 30% glycerol and the wash/elution buffers for affinity purification included 20% glycerol (instead of 5%). These modifications improved the polydispersity of the SEC profile with HCN2SM, although the profile still exhibited significant aggregation in the affinity purified material. Only the peak SEC fraction (containing 30-50 nM protein) was used for our studies and binding measurements were performed within 2-6 h of the final protein purification step (Extended Data Fig. 1c).

Although the extraction and affinity steps of HCN1SM and HCN2SM used different detergents, the final purification step included exchanging both proteins into 0.1 mM GDN during SEC. The only difference in the final conditions for HCN1SM and HCN2SM is the glycerol content which was adjusted to enhance monodispersity—a widely used measure of protein stability—in the SEC profile. Prior to single-molecule imaging, HCN1SM and HCN2SM were extensively washed in glycerol free GDN containing SEC buffer. All single-molecule data were collected under identical buffer conditions for HCN1SM and HCN2SM. We note that the relative differences in estimated binding affinities of intact HCN isoforms from single-molecule data match those reported for the soluble CNBDs⁴⁵.

ZMW fabrication

ZMWs were fabricated at the Center for Nanophase Materials Sciences facility at Oak Ridge National Lab using positive-tone electron-beam lithography⁴. Cover glasses (Fisher Scientific cat. no. 12-548-C, 130-170 μm thickness) were cleaned by soaking in 5 parts deionized water, 1 part 30% hydrogen peroxide, 1 part 35% ammonium hydroxide for 15 min at 75 °C. Substrates were rinsed, dried with N₂ gas, and plasma-cleaned with a Harrick PDC-32G for 10 min to remove any remaining organic impurities on the surface. The substrates were coated with thermally evaporated aluminium at a rate of 2 Å s⁻¹ using a JEOL dual source E-beam evaporator to a final thickness of 100 nm. Substrates were spin-coated with the positive tone electron-beam photoresist ZEP520A (ZEONREX Electronic Chemicals) for 45 s at 2,000 rpm followed by baking for 2 min at 180 °C. ZMW features of 150-nm-diameter dots were patterned using JEOL JBX-9300FS E-beam lithography system with a base dose of 450 μ C cm⁻², 100 kV acceleration voltage, and 2 nA beam current. Following exposure, substrates were developed in xylenes for 30 s, rinsed with isopropyl alcohol, and dried with N₂. One hundred nanometres of aluminium was dry etched in an Oxford Plasmalab System 100 Reactive Ion Etcher with a mixture of 30 standard cubic centimeters (sccm) chlorine (Cl₂) and 10 sscm boron trichloride (BCl3) gasses at 50 °C for 60 s. Following etching, the substrates were plasma cleaned with a Harrick PDC-32G for 15 min on a high setting to remove remaining photoresist. This resulted in arrays of round ZMW wells of 150 nm diameter and 2 μm pitch. Each ZMW chip used in this study (n=7) was visualized with SEM to confirm fabrication quality, diameter, and pitch (example in Fig. 1a).

Imaging chamber preparation

Cover glasses intended for photobleaching experiments via TIRFM and not ZMW fabrication were cleaned by successive sonication for 60 min in 2% Hellmanex (Hellma), HPLC-grade ethanol (Millipore Sigma) and 1 M KOH, with deionized water rinses between solution exchanges. Both cover glasses and ZMW chips were additionally plasma cleaned for 5 min before surface functionalization. For ZMWs, the Allayer was passivated by incubation in 2% poly(vinylphonic acid) (PVPA) (Polysciences) for 3 min 90 °C, followed by rinsing with Milli-Q ultrapure water and drying with Ar gas³⁸. A silicone-gasketed chamber was attached to each substrate to hold small volumes and reduce evaporation (SecureSeal Hybridization Chambers, Grace Bio-Labs). Both cover glasses and ZMW chips were silanized overnight in 2 mg ml⁻¹ biotin-PEG-silane (molecular mass = 3,400 g mol⁻¹) and 10 mg ml⁻¹ mPEG-silane (molecular mass = 2,000 g mol⁻¹) (Laysan Bio) in HPLC-grade ethanol (Millipore Sigma) with 5% glacial acetic acid. Samples were rinsed thoroughly with HPLC-grade ethanol, Milli-Qultrapure water, and dried with Ar gas. Samples were additionally incubated with 10 mg ml⁻¹ bovine serum albumin (BSA) in tris buffered saline (TBS: 300 mM NaCl, 20 mM Tris HCl, pH 7.9) for 30 min to ensure robust passivation.

Single-molecule imaging

Single-molecule fluorescence imaging was performed on an inverted microscope (Olympus, IX-71) with a high NA oil immersion objective (Olympus, 100X, 1.49 NA) and controlled by Metamorph software (Molecular Devices). Laser excitation at either 488 nm or 532 nm (Coherent, Sapphire LP) was fed into a single AOTF (Laser Launch) and guided into a single-mode fibre (Thorlabs). The beam was collimated with an achromatic lens (Thorlabs), passed through a quarter-wave plate (Thorlabs), and focused on the objective's back aperture with another achromatic lens (Thorlabs). The power of each beam into the objective was measured at about 5.3 mW for 488 nm and 6.7 mW for 532 nm, and the spot size at the sample plane was approximately 50 µm in diameter. Excitation and emission were filtered using two different dichroic and filter cubes applied separately (Semrock Brightline, LF488-C-000, Cy3/ Cy5-A-OMF for fcAMP) and imaged on a 512 × 512 EMCCD (Andor iXon Ultra X-888) at 10 Hz. This set-up enabled simultaneous recording of about 1,600 ZMWs at a time in an approximately $80 \times 80 \,\mu m$ field of view (Extended Data Fig. 2a).

All single-molecule experiments were carried out in TBS supplemented with 1 mg/ml BSA, 100 μ M GDN, and 5 mM DTT. Biotinylated cover glasses and ZMWs were sequentially incubated with 1 μ M streptavidin (Prospec, cat. no. PRO-791) and 10 nM biotinylated GFP-TRAP (ChromoTek) for 10 min each. Purchased GFP-TRAP was provided at 1 mg ml $^{-1}$ (molecular mass = 13.9 kDa) and diluted to 10 nM in TBS before use (1:7,200 dilution). GFP tagged HCN1SM/HCN2SM molecules were pulled down to the surface by incubation at either 5 pM (cover glasses) or 250 nM (ZMW) for 10 min then thoroughly rinsed to remove freely diffusing eGFP–HCN1/2 before imaging. The specificity of the GFP-TRAP for tethering HCN1SM and HCN2SM was confirmed using a non-specific binding assay (Extended Data Fig. 2a). The manufacturer reports a K_d =1 pM for GFP-TRAP–GFP interaction. We did not observe any noticeable decrease in single-molecule spots over a typical imaging session (1–2 h) indicating HCN1SM and HCN2SM remain surface tethered.

For binding experiments, TBS was first purged with argon for 30 min (before BSA, DTT, or GDN addition), and further supplemented with 2 mM Trolox, 2.5 mM protocatechuic acid (PCA, Millipore Sigma), and various concentrations of 8-(2-[DY-547]-aminoethylthio) adenosine-3′,5′-cyclic monophosphate (fcAMP; BioLog cat. no. 109-001). Prior to 532 nm excitation, an additional 250 nM protocatechuate 3,4-dioxygenase from *Pseudomonas* sp. (PCD, Millipore Sigma) was added to complete the oxygen scavenging system. All solutions were replenished every 30 min to minimize evaporation and ensure the oxygen scavenging system was active. The specicity of fcAMP binding

to surface tethered HCN1SM and HCN2SM was confirmed using a non-specific binding assay with 1 μ M fcAMP in the absence of HCN1SM/HCN2SM and after the addition of 1 mM cAMP (Extended Data Fig. 2c, d). Proteins were sparsely deposited onto the array to reduce the probability of having more than one protein per ZMW. On average, 313 \pm 188 ZMWS were occupied per field of view. Considering Poisson statistics for single-molecule deposition into ZMWs, the observed deposition rate (λ = 0.22) leads us to only anticipate about 2% of ZMWs per field of view to contain more than one protein.

All ligand-binding experiments used fcAMP, a fluorescent derivative of cAMP featuring a DY-547 fluorophore. This analogue activates HCN2 channels with a similar efficiency to cAMP 2,12 . A co-localization paradigm was used to identify ZMWs featuring HCN molecules receptive to fcAMP binding. First, the array was excited with a 488 nm pump to identify ZMWs containing at least one HCN molecule. Excitation at 488 nm was continued to photobleach the eGFP tags (114 \pm 87 s). Diffusing fcAMP was then continuously excited at 532 nm for at least 300 s with a 100-ms exposure time to monitor binding activity.

Single-molecule analysis

Single-molecule fluorescence time trajectories were extracted from tiff stacks saved by Metamorph (Molecular Devices) using MATLAB (Mathworks). Locations of single molecules were identified by eGFP emission. For each image stack, a binary image mask was created by averaging the first 100 images, removing background with a top-hat filter and thresholding. Identified locations with an area greater than 4-pixels and at least 5-pixel separation between all neighbouring locations were considered a region of interest (ROI). ROI locations were refined using a 2D Gaussian to fit the local intensity height map on the averaged image. For co-location experiments of fcAMP binding using ZMWs, ROIs identified in the 488-nm channel (eGFP photobleaching steps) were linearly transformed to the 532-nm channel (fcAMP) followed by 2D Gaussian refinement. The time-dependent fluorescence at each ROI was obtained by projecting the average image intensity in a 7×7 -pixel square centred around the ROI for each image of the stack. The first 50 frames (5 s) of each time series were removed to account for a fluorescence decay inside the ZMW upon initial illumination (see raw data in Extended Data Figs. 2d, 3, 4). No baseline, background, or drift corrections were applied to the trajectories. To assess whether photobleaching was affecting our estimated kinetic parameters, we correlated the intensity of each isolated-B1 event with its dwell time for HCN1SM and HCN2SM across each fcAMP concentration (Extended Data Figs. 6, 7). Although excitation intensity varied across the field of view, we do not observe a correlation with binding kinetics which suggests photobleaching is not impacting our estimations of the kinetic parameters.

The divisive segmentation and clustering (DISC) algorithm was applied to each fcAMP binding trajectory for an unbiased detection of discrete states (number of ligands bound) and transitions³⁶. States are identified in DISC using a top-down unsupervised clustering algorithm and transitions are determined using the Viterbi algorithm. All idealized traces were visually inspected following idealization. Traces featuring greater than five discrete states and/or low signal to noise ratios were removed from analysis. Single change-point detection was applied to truncate traces exhibiting an asynchronous decay of activity over time, a phenomenon previously observed in both bulk and single-molecule studies which may be caused by free oxygen radicals modifying CNBDs ^{36,48}. Minor heterogeneity in event fluorescence intensities is observed, probably deriving from dye photophysics, and is effectively handled by the DISC algorithm³⁶. In total, our analysis includes 2.2 × 10⁵ seconds (60 h) of HCN1 activity across 739 molecules (1.8×10^5) events) at fcAMP concentrations between 0.1 to 0.9 μ M, and 1.26×10^5 seconds (35 h) of HCN2 activity across 444 molecules (8.2 × 10^4 events) at fcAMP concentrations between 0.1 to 1.5 µM (Supplementary Table 1). These results are drawn from different protein preparations

(HCN1SM: n = 2, HCN2SM: n = 3) and collected across multiple ZMW chips (HCN1SM: n = 3, HCN2SM: n = 4). All statistical analysis was performed using MATLAB 2019b unless otherwise stated. Errors are reported as s.d., s.e.m. or 95% confidence intervals and are indicated in each caption. All analyses were additionally repeated after removing single-frame (100-ms) events to account for missed events, blinking, diffusion, or noise (Supplementary Methods, Supplementary Table 7).

Maximum likelihood estimations of state occupancy distributions, photobleaching steps distributions, and dwell time distributions were all performed using custom scripts in MATLAB. For state occupancy distributions (Fig. 2a, Extended Data Fig. 5, Supplementary Table 2), the total number of observed frames spent in each state across all molecules at given fcAMP concentration was treated as binomial distribution. Here, for 4 identical bindings sites, each with a probability of ligand binding P, the probability of x binding sites being occupied simultaneously is

$$Pr(x) = \frac{4!}{x!(4-x)!}P^{x}(1-P)^{4-x}$$

Distributions of photobleaching steps (Extended Data Fig. 1c, d) were treated as a zero-truncated binomial distribution to account for the inability to observe molecules wherein all subunits were photobleached before excitation. For 4 identical eGFP tags, each with a probability of being fluorescent P, the probability of observing x photobleaching steps is given by

$$Pr(x) = \frac{4!}{x! (4-x)!} \left(\frac{P^x (1-P)^{4-x}}{1 - (1-P)^4} \right)$$

Dwell time distributions of unbinned isolated-B1 events (Fig. 3, Extended Data Figs. 6, 7, Supplementary Table 3) were treated as a mono- or biexponential distribution. The probability of observing a dwell time of duration \boldsymbol{x} is given by

$$Pr(x) = \sum_{i=1}^{z} A_i \tau_i e^{-\tau_i x}$$

in which z is the number of exponentials being fit, A is the fitted amplitude where $\sum_{i=1}^{n} A_i = 1$, and τ the fitted time constants. A log likelihoodratio test was performed for each dwell time distribution to compare the goodness-of-fit of single and double exponential distributions. The homogeneity of the estimated parameters within the full population of molecules was confirmed by an outlier analysis (Extended Data Fig. 8, Supplementary Methods). Dwell time distributions are visualized in two ways. First, dwell times are binned and plotted as histograms where the abscissa values correspond to the centre of the bars. Second, isolated-B1 dwell times are additionally visualized as probability density function (PDF) plotted on a log scale to highlight the long-lived dwell times (see insets of Extended Data Figs. 3, 6, 7). The PDF values are computed by dividing each bin by the product of the bin width and the total number of counts. Error bars for each bin were calculated as the error of binomial distribution, previously described elsewhere26.

HMM analysis

HMM analysis of idealized data sets for HCN1SM and HCN2SM were performed with $QuB^{42,43}$. The first and last event of each trajectory

was removed before analysis to avoid interpretation of truncated events. Models were globally optimized to simultaneously describe the idealized binding events for all molecules across all fcAMP concentrations using maximum idealized point (MIP) likelihood rate estimation. The optimized transition rates returned by QuB are reported as mean \pm s.e.m. The goodness of fit of each model was assessed by Bayesian information criterion⁴⁴

$$BIC = k \times ln(n) - 2 \times LL$$

in which k is the number of free parameters in the model (Supplementary Table 4), n is the total number data points (frames) across all fcAMP concentrations (Supplementary Table 1), and LL is the log likelihood by MIP estimation in QuB⁴². The model with the lowest Bayesian information criterion value was considered the best fit (Supplementary Table 4). Optimized rates for all models are also in Supplementary Table 5. The data were additionally resampled to ensure homogeneity (Supplementary Methods, Supplementary Table 6).

Reporting summary

Further information on research design is available in the Nature Research Reporting Summary linked to this paper.

Data availability

All experimental data are available upon reasonable request. Source data are provided with this paper.

Code availability

The DISCO software package is available at https://github.com/ChandaLab/DISC and fully described elsewhere³⁶. All additional MATLAB scripts for single-molecule analysis and image processing are available upon reasonable request.

- Goehring, A. et al. Screening and large-scale expression of membrane proteins in mammalian cells for structural studies. Nat. Protoc. 9, 2574–2585 (2014).
- Idikuda, V. et al. Singlet oxygen modification abolishes voltage-dependent inactivation of the sea urchin spHCN channel. J. Gen. Physiol. 150, 1273–1286 (2018).

Acknowledgements This research was supported by the NIH grants to B.C. (NS-116850, NS-101723, and NS-081293), D.S.W. (T32 fellowship GM007507) and NSF to R.H.G. (CHE-1856518). We thank K. A. Knapper and C. H. Vollbrecht for assistance with cover glass cleaning at the Wisconsin Centers for Nanoscale Technologies; M. P. Goldschen-Ohm and M. Smith for helpful discussions; C. Lingle and L. Anson for their feedback on the manuscript; and M. Jackson for sparking this collaboration. ZMWs were fabricated at the Center for Nanophase Materials Sciences at Oak Ridge National Laboratory, which is a DOE Office of Science User Facility.

Author contributions D.S.W., S.C., R.H.G. and B.C. conceived and designed the studies; V.I. performed electrophysiology experiments; S.C. performed molecular biology and protein purification; D.S.W. and R.Z. performed single-molecule experiments; D.S.W. analysed single-molecule data. D.S.W. fabricated ZMWs under supervision of S.T.R.; D.S.W., S.C., R.H.G. and B.C. wrote the manuscript with input from others.

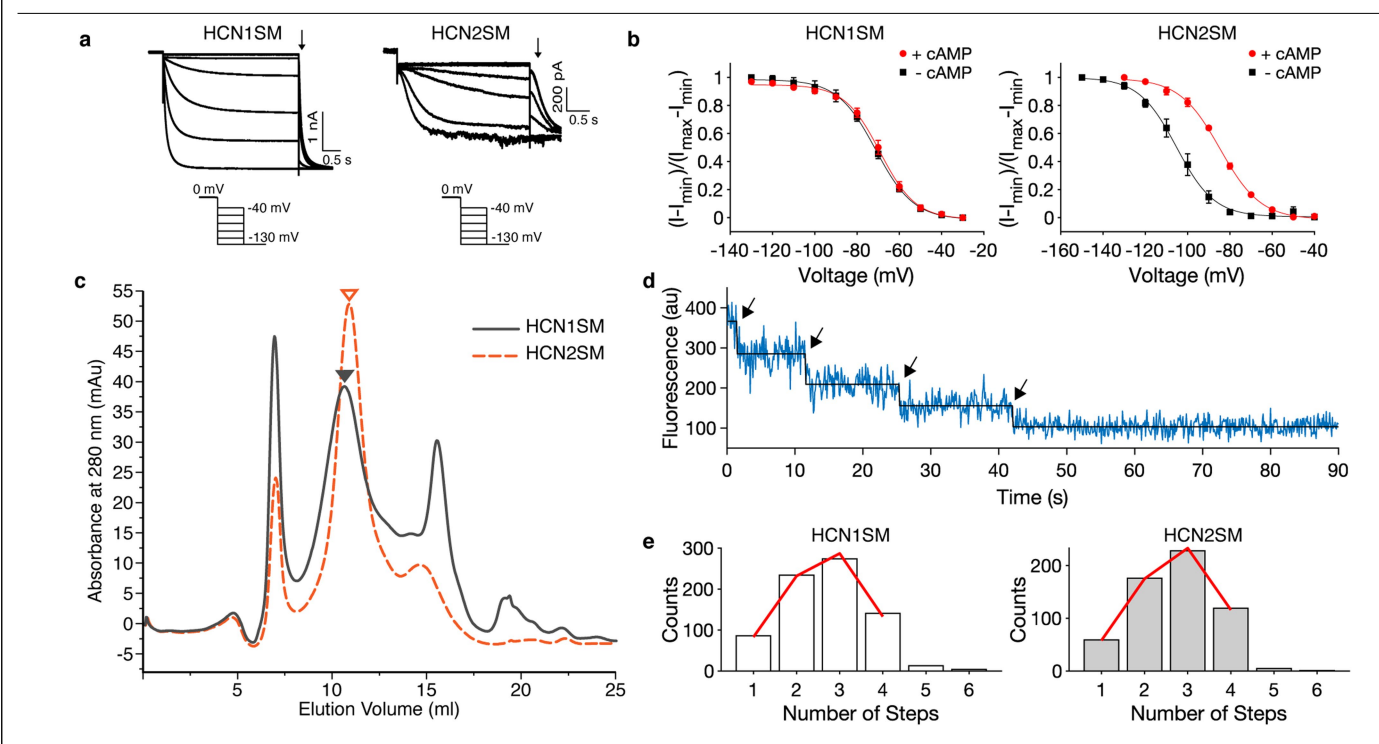
Competing interests The authors declare no competing interests.

Additional information

Supplementary information The online version contains supplementary material available at https://doi.org/10.1038/s41586-021-03686-x.

Correspondence and requests for materials should be addressed to R.H.G. or B.C. **Peer review information** *Nature* thanks the anonymous, reviewer(s) for their contribution to

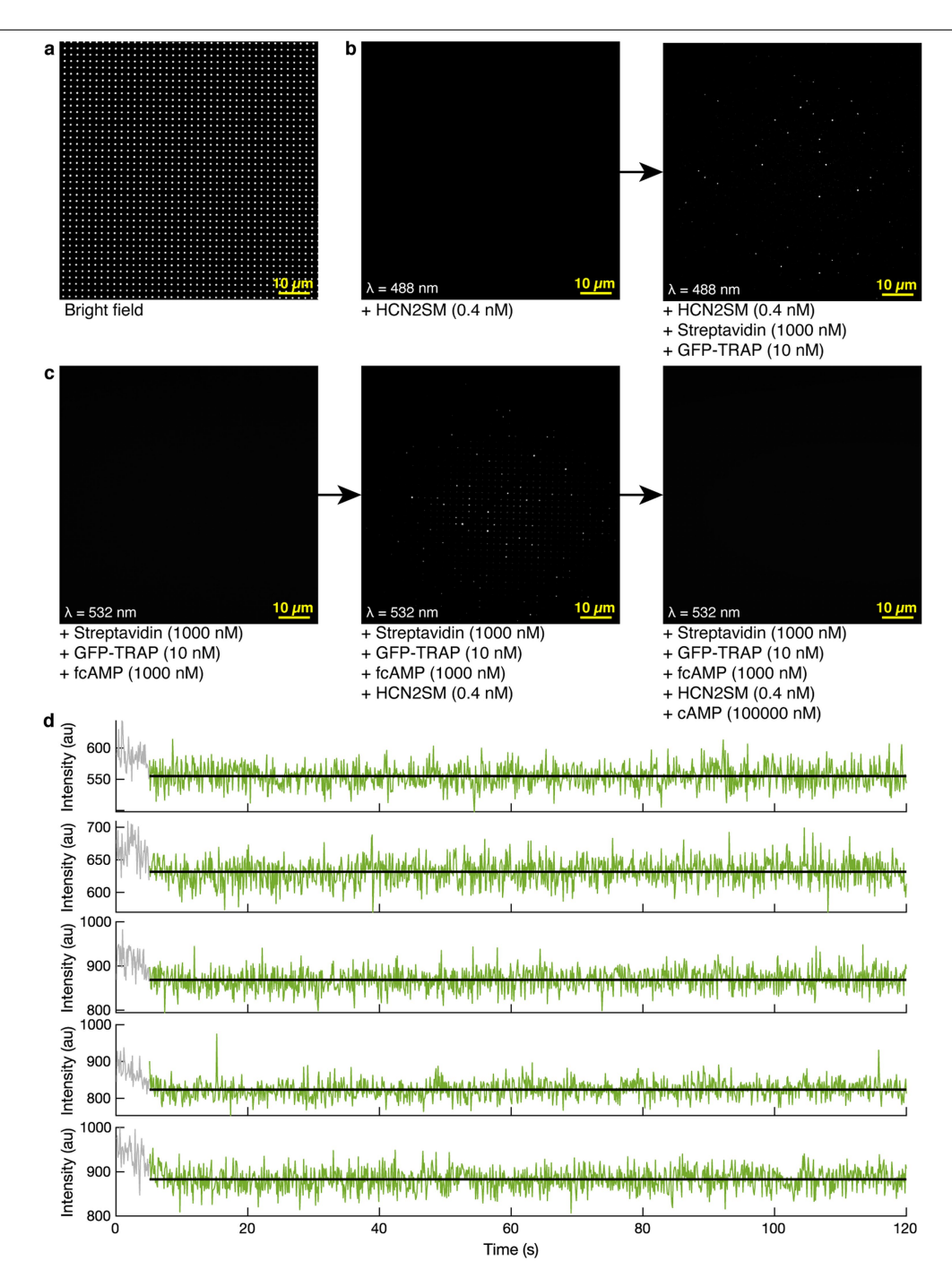
the peer review of this work. Peer reviewer reports are available. **Reprints and permissions information** is available at http://www.nature.com/reprints.



Extended Data Fig. 1 | Characterization of HCN1SM and HCN2SM.

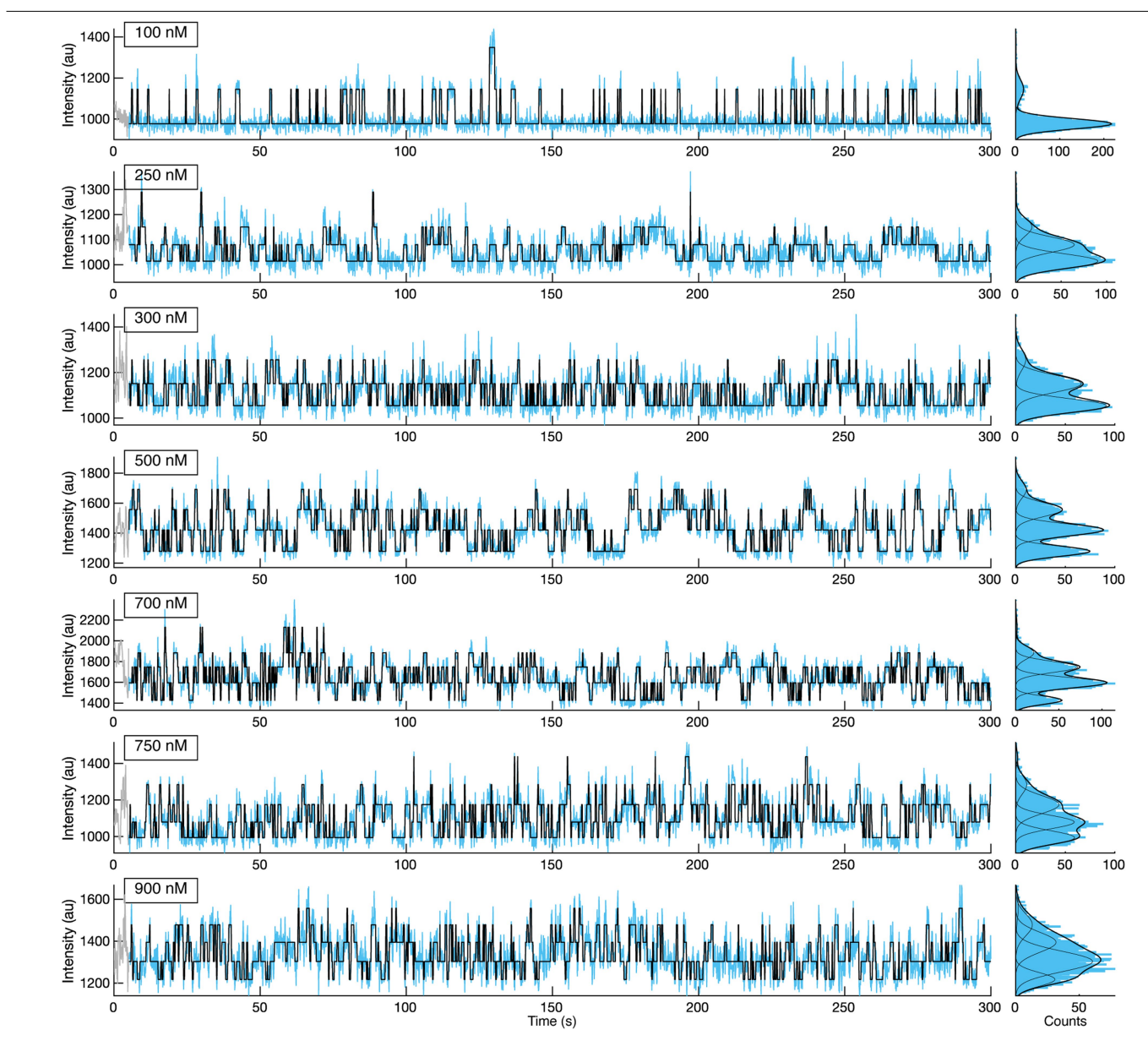
a, Representative electrophysiological recordings (top) of HCN1SM (left) and HCN2SM (right) with voltage protocol. Tail currents (arrow) were collected at $-130\,$ mV and were used to generate the activation curves. b, Normalized activation curves of HCN1SM (left) and HCN2SM (right) in the absence or presence of saturating concentrations (500 μ M) of internal cAMP with a Boltzmann fit (red). Data points are mean \pm s.e.m. (n=5 patches). $V_{\rm I/2}$ values for are HCN1SM-71.2 \pm 0.4 mV without cAMP and $-69.1\pm$ 0.5 mV with cAMP. $V_{\rm I/2}$ values for are HCN2SM-105.2 \pm 0.6 mV without cAMP and $-84.6\pm$ 0.5 mV with cAMP).

c, Size exclusion chromatography (SEC) profiles of HCN1SM (grey) and HCN2SM (orange dashed). Triangles indicate the peak fraction (0.3 ml) used for single-molecule measurements. **d**, Example fluorescence vs time trajectory of photobleaching eGFP-tagged HCN2SM tetramers via TIRFM. **e**, Distributions of photobleaching steps overlaid with a maximum likelihood estimate of a zero-truncated binomial distribution (red) for a tetrameric complex with a probability (P) of observing eGFP (HCN1: P = 0.65, 95% CI [0.63, 0.67], n = 752; HCN1: P = 0.67, 95% CI [0.65, 0.69], n = 588).

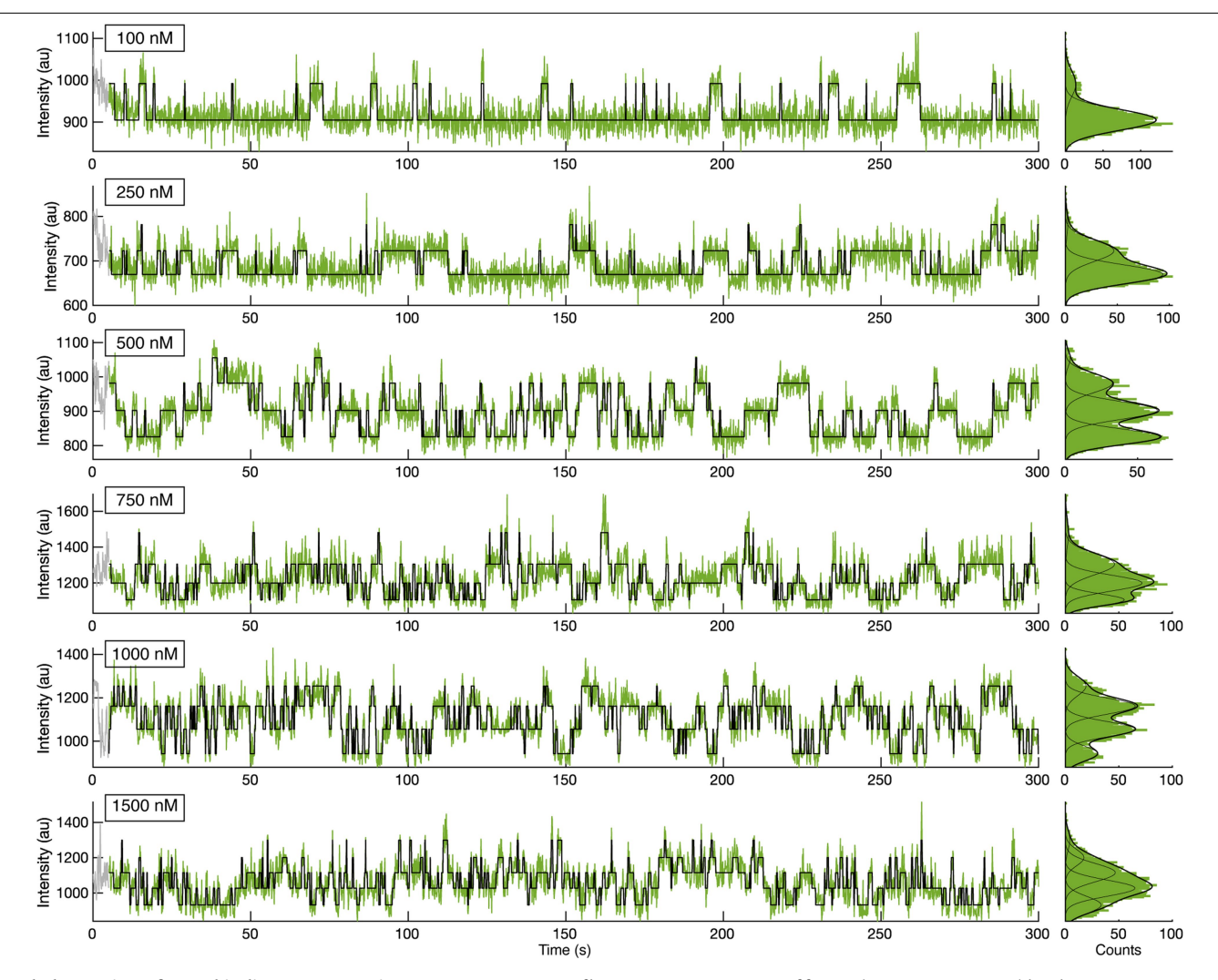


Extended Data Fig. 2 | **Non-specific binding in ZMWs. a**, Bright field image of ZMW array on single-molecule imaging set-up featuring a 512×512 pixel EMCCD and a $100 \times$ objective. Each white dot (about 1,600 per field of view) is a ZMW. **b**, **c**, Test of specific binding of eGFP-tagged HCN2SM to ZMWs (**b**) and of fcAMP (**c**) to HCN2SM in ZMWs. For **b** and **c**, all images shown are averaged over

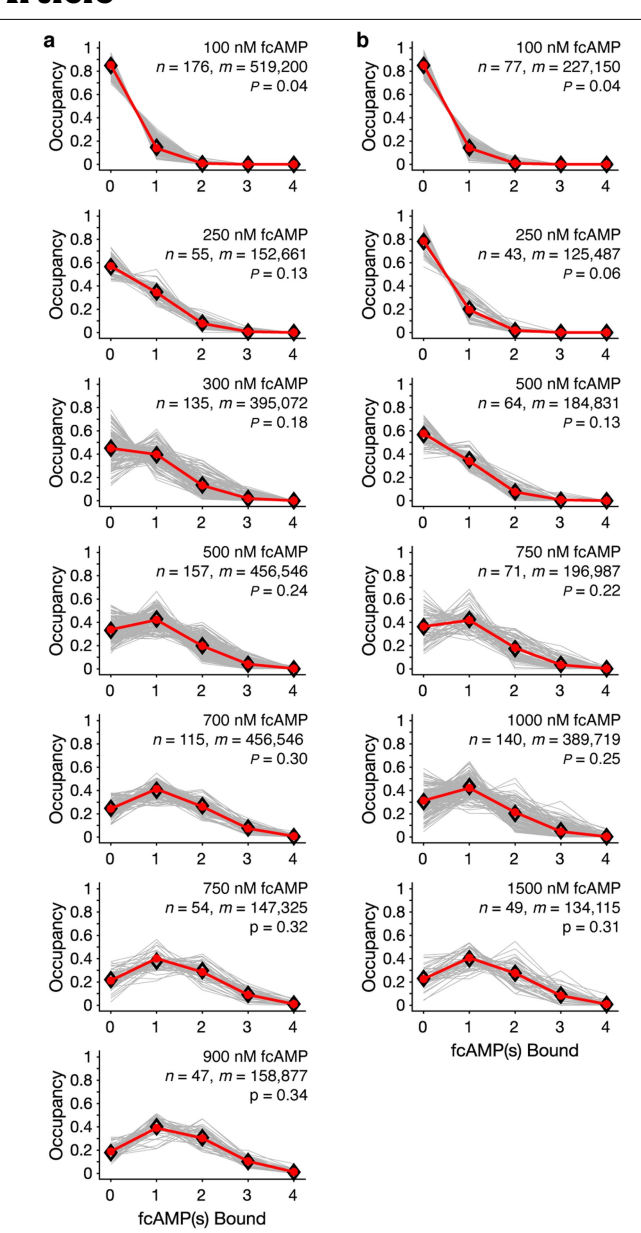
the first 10 frames (1 s) and background subtracted for visualization. Brightness and contrast were adjusted for clarity. \mathbf{d} , Representative and randomly selected fluorescence trajectories of empty (no HCN) and passivated ZMWs with 1,000 nM fcAMP fit with DISC (black). The first 50 frames (grey) were removed from analysis.



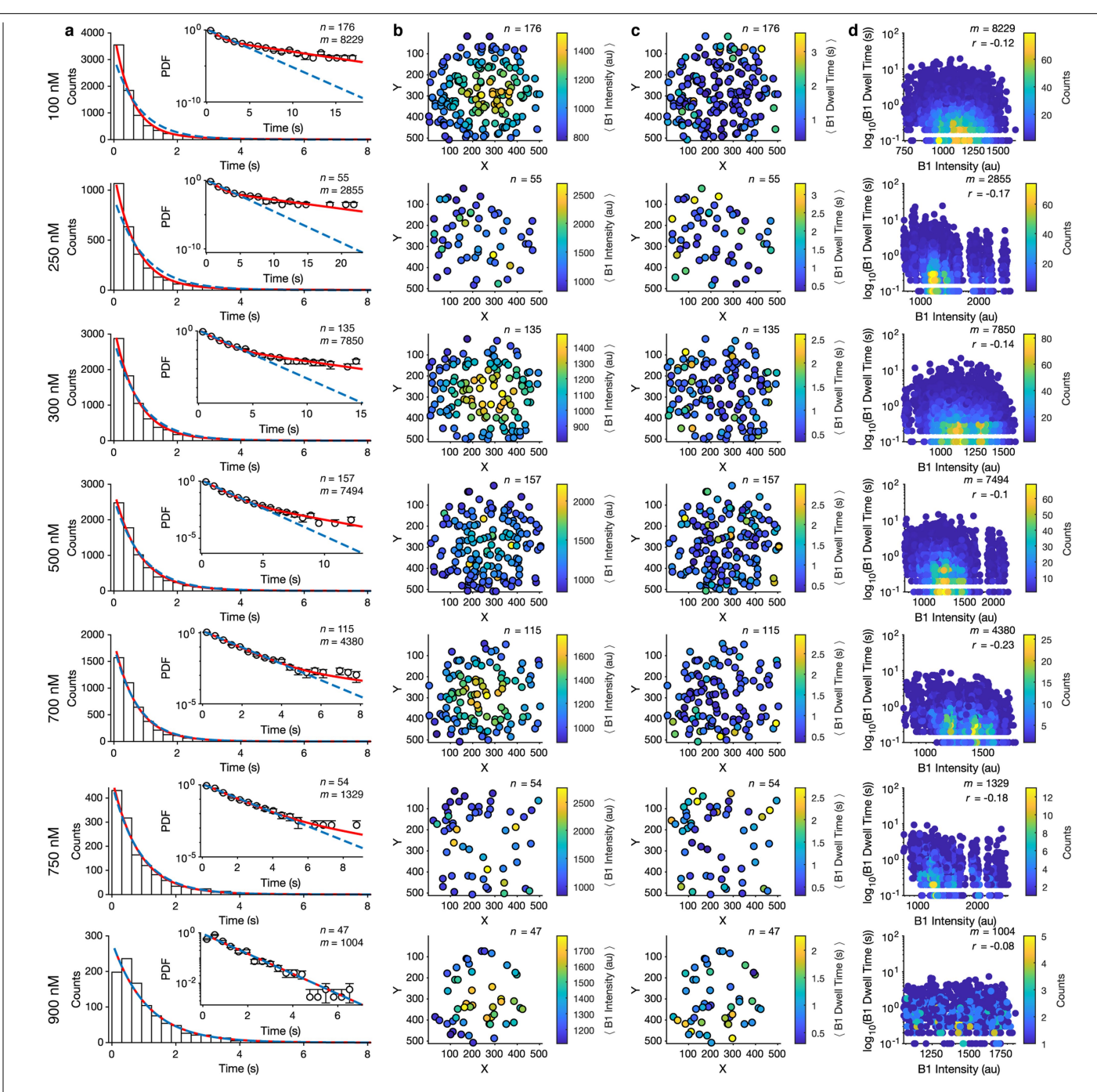
 $\textbf{Extended Data Fig. 3} | \textbf{fcAMP binding to HCN1SM in ZMWs.} \ Representative fluorescence trajectories of fcAMP (100 nM to 900 nM) binding to HCN1SM in ZMWs with idealized fits (black) imaged at 100-ms resolution. The first 50 frames (grey) were removed from analysis.$



 $\textbf{Extended Data Fig. 4} \ | \ \textbf{fcAMP binding to HCN2SM in ZMWs.} \ \text{Representative fluorescence trajectories of fcAMP (100 nM to 1,500 nM) binding to HCN2SM in ZMWs with idealized fits (black) imaged at 100-ms resolution. The first 50 frames (grey) were removed from analysis.$

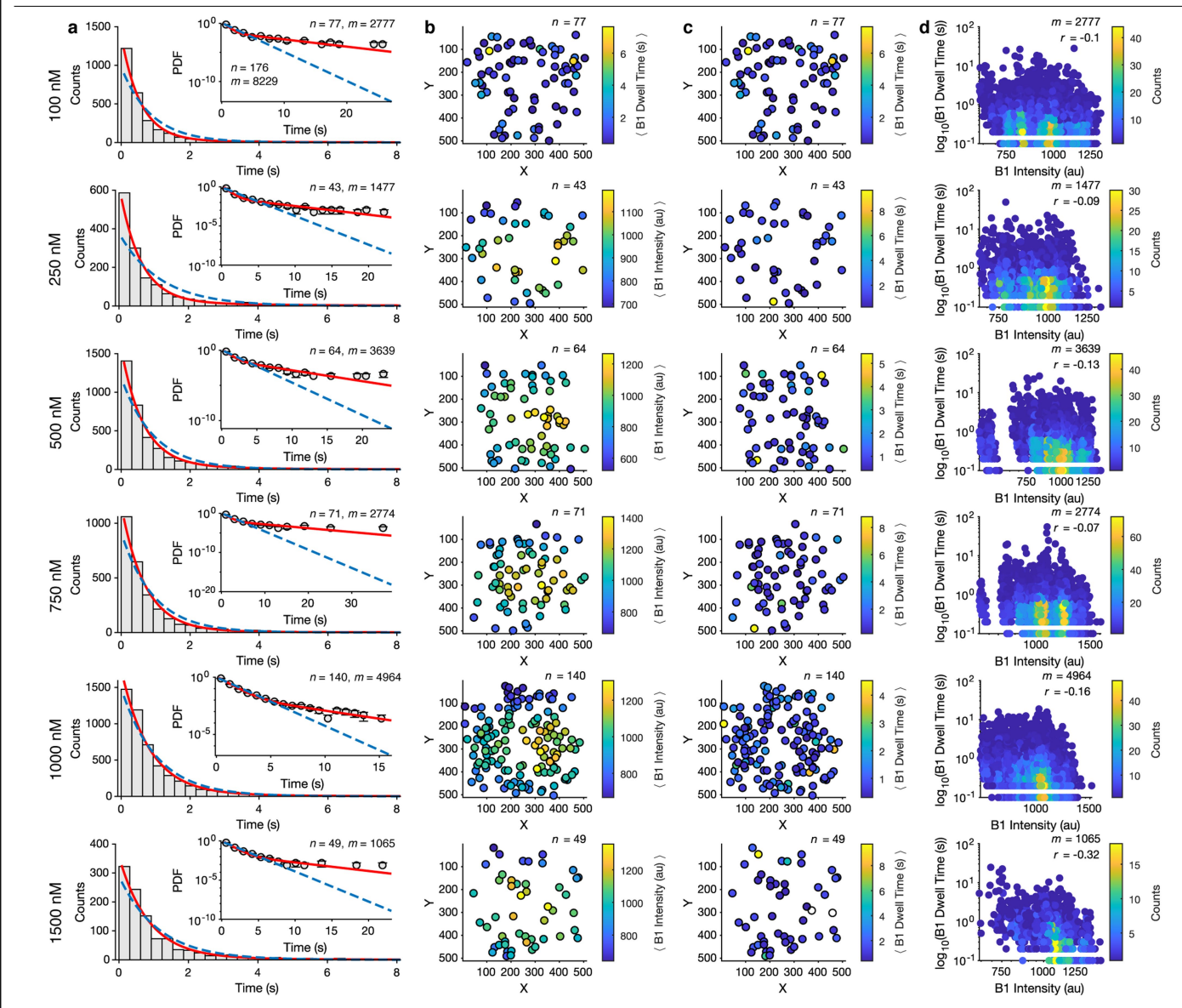


Extended Data Fig. 5 | **All state occupancy distributions. a, b,** Normalized state occupancy distributions for HCN1SM (**a**) and HCN2SM (**b**) across all recorded fcAMP concentrations. Each plot indicates the total number of molecules (n) and data points (that is, frames, m) included in the analysis. P is the success rate of the optimized binomial distribution considering four binding sites. All obtained and expected state occupancies values are in Supplementary Table 2.



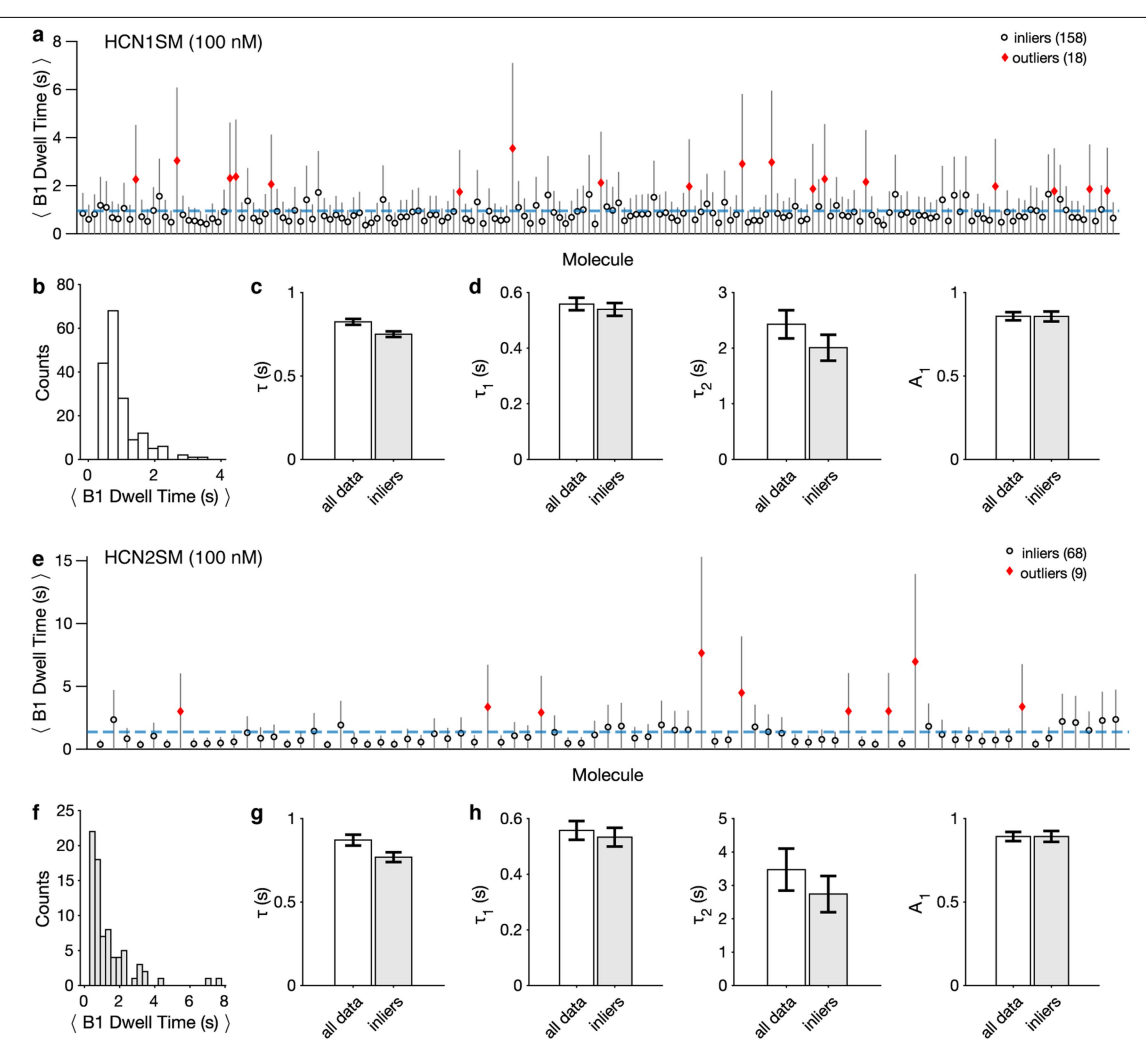
Extended Data Fig. 6 | **Isolated-B1 Events of HCN1SM. a**, Dwell time distributions of isolated-B1 events for HCN1SM at various fcAMP concentrations overlaid with maximum likelihood estimates for monoexponential (blue dashed) and biexponential (red) distributions (Supplementary Table 3). For inset, error bars are the error of a binomial distribution (Methods). **b, c**, Coordinates of identified single-molecules in the

 512×512 pixel field of view superimposed across all ZMW arrays. The colour bars denote the average dwell time (**b**) and fluorescence (**c**) of the isolated-B1 state for each molecule (*n*). **d**, Correlation of fluorescence intensity and dwell times for each isolated-B1 event (*m*), where *r* is the Pearson correlation coefficient. Data are binned for visualization.



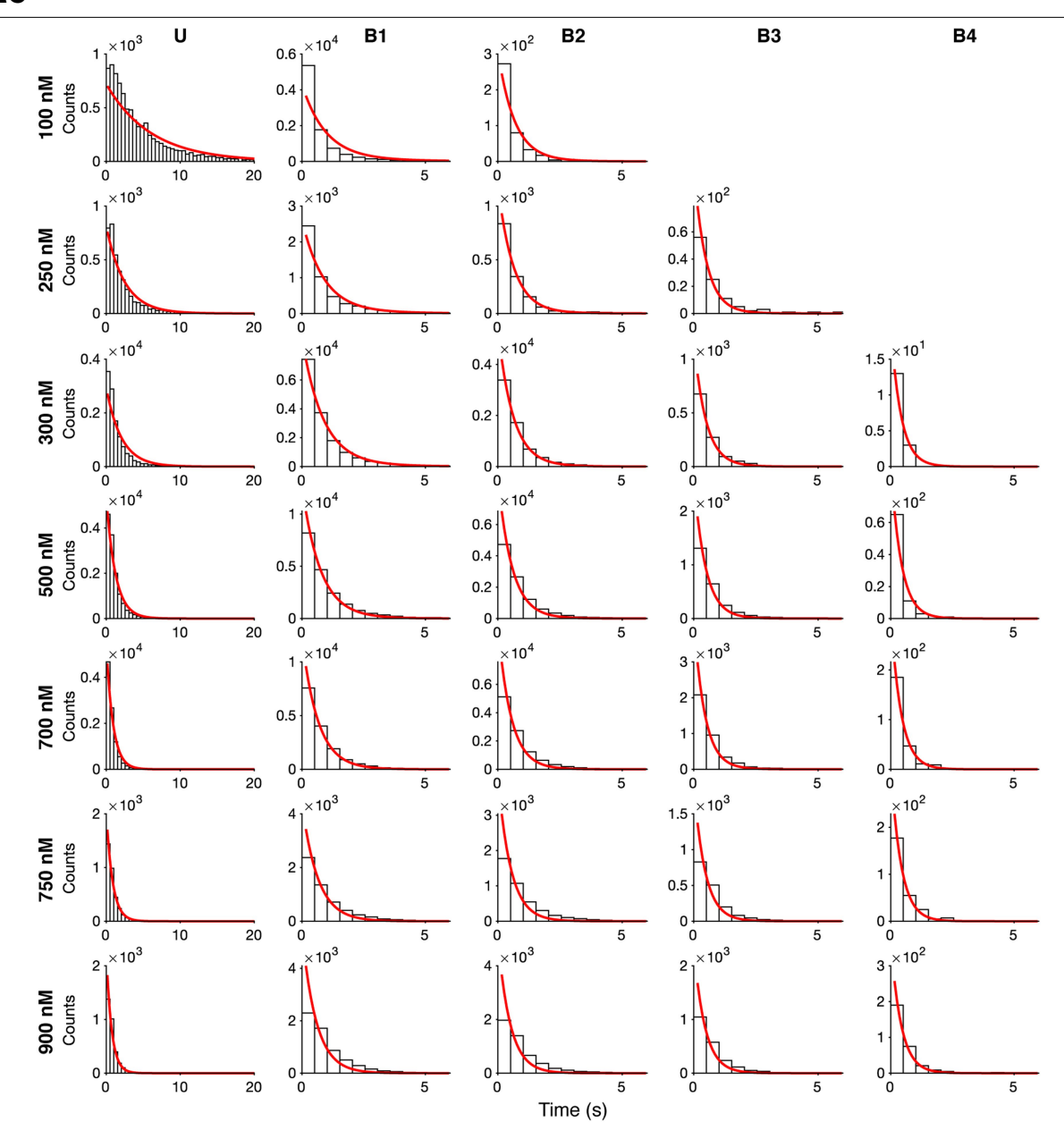
Extended Data Fig. 7 | **Isolated-B1 Events of HCN2SM. a**, Dwell time distributions of isolated-B1 events for HCN2SM at various fcAMP concentrations overlaid with maximum likelihood estimates for monoexponential (blue dashed) and biexponential (red) distributions (Supplementary Table 3). For inset, error bars are the error of a binomial distribution (Methods). **b, c**, Coordinates of identified single-molecules in the

 512×512 pixel field of view superimposed across all ZMW arrays. The colour bars denote the average dwell time (**b**) and fluorescence (**c**) of the isolated-B1 state for each molecule (*n*). **d**, Correlation of fluorescence intensity and dwell times for each isolated-B1 event (*m*), where *r* is the Pearson correlation coefficient. Data are binned for visualization.

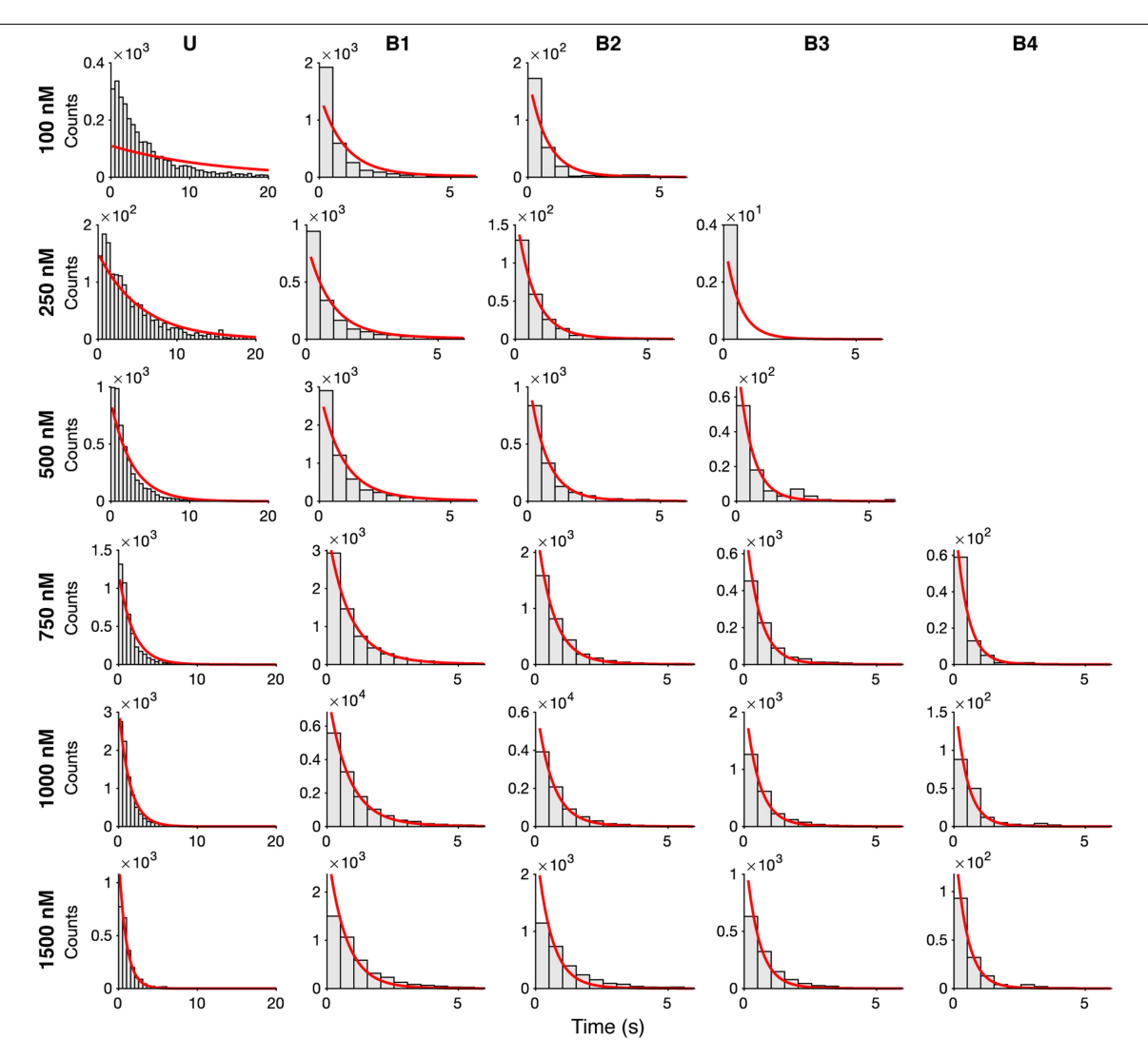


Extended Data Fig. 8 | Isolated-B1 events do no exhibit static heterogeneity. a, e, Average isolated-B1 dwell time of HCN1SM (a) and HCN2SM (e) for each molecule at 100 nM fcAMP. Outliers (diamonds) were identified by three scaled median absolute deviations. Data plotted as mean \pm s.d. of exponential distribution. The blue dashed line indicates the average B1 dwell time across all molecules (HCN1SM: n=176; HCN2SM: n=77). b, f, Histograms of average isolated-B1 dwell times for each HCN1SM (b) and HCN2SM (f) molecule. c, g, Parameters for a monoexponential fit (τ) to

isolated-B1 dwell times of HCN1SM (\mathbf{c}) and HCN2SM (\mathbf{g}). \mathbf{d} , \mathbf{h} , Parameters for a biexponential fit (τ_1 , τ_2 , A_1) to isolated-B1 dwell times of HCN1SM (\mathbf{d}) and HCN2SM (\mathbf{h}). For \mathbf{c} , \mathbf{g} , \mathbf{d} , \mathbf{h} , the ordinate corresponds to the obtained parameter (τ , τ_1 , τ_2 , A_1) and error bars are 95% confidence intervals. All parameters were obtained using maximum likelihood estimates across all isolated-B1 events in either all data (HCN1SM: n=8,229; HCN2SM: n=2,676) or inlier (HCN1SM: n=7,816; HCN2SM: n=2,575) groups, as indicated on the abscissa.



Extended Data Fig. 9 | HCN1SM dwell time distributions. Dwell time distributions of all liganded states of HCN1SM across all fcAMP concentrations overlaid with expectations from the optimized rates in Fig. 4b.



 $\textbf{Extended Data Fig. 10} \ | \ \textbf{HCN2SM dwell time distributions.} \ D \ well time \ distributions of all \ liganded states of \ HCN2SM \ across \ all \ fcAMP \ concentrations \ overlaid \ with \ expectations \ from \ the \ optimized \ rates \ from \ in \ Fig. 4b.$



| Corresponding author(s): F | Randall H. Golsmith & Baron Chanda |
|----------------------------|------------------------------------|
|----------------------------|------------------------------------|

Last updated by author(s): May 6, 2021

Reporting Summary

Nature Research wishes to improve the reproducibility of the work that we publish. This form provides structure for consistency and transparency in reporting. For further information on Nature Research policies, see <u>Authors & Referees</u> and the <u>Editorial Policy Checklist</u>.

For all statistical analyses, confirm that the following items are present in the figure legend, table legend, main text, or Methods section

| ~ | | | | | |
|---|----|----|-----|----|----|
| 5 | ta | ŤΙ | IS: | ŀι | CS |

| 1 Of all 3 | statistical analyses, commit that the following items are present in the figure regend, table regend, main text, or internous section. |
|------------------|--|
| n/a Co | onfirmed |
| | The exact sample size (n) for each experimental group/condition, given as a discrete number and unit of measurement |
| | A statement on whether measurements were taken from distinct samples or whether the same sample was measured repeatedly |
| | The statistical test(s) used AND whether they are one- or two-sided Only common tests should be described solely by name; describe more complex techniques in the Methods section. |
| $\boxtimes \Box$ | A description of all covariates tested |
| $\boxtimes \Box$ | A description of any assumptions or corrections, such as tests of normality and adjustment for multiple comparisons |
| | A full description of the statistical parameters including central tendency (e.g. means) or other basic estimates (e.g. regression coefficient) AND variation (e.g. standard deviation) or associated estimates of uncertainty (e.g. confidence intervals) |
| | For null hypothesis testing, the test statistic (e.g. <i>F</i> , <i>t</i> , <i>r</i>) with confidence intervals, effect sizes, degrees of freedom and <i>P</i> value noted <i>Give P values as exact values whenever suitable.</i> |
| $\boxtimes \Box$ | For Bayesian analysis, information on the choice of priors and Markov chain Monte Carlo settings |
| $\boxtimes \Box$ | For hierarchical and complex designs, identification of the appropriate level for tests and full reporting of outcomes |
| | $\ \ \ \ \ \ \ \ \ \ \ \ \ \ \ \ \ \ \ $ |
| · | Our web collection on <u>statistics for biologists</u> contains articles on many of the points above. |
| Softv | vare and code |

Policy information about availability of computer code

Data collection

Single-molecule images collected using MetaMorph (version 7.8.10.0, Molecular Devices). Electrophysiology data collected using pCLAMP (version 10.7, Molecular Devices)

Data analysis

Electrophysiology data were analyzed using OriginPro (version 2020b, OriginLab). Single-molecule were analyzed using custom scripts in MATLAB (2019b, MathWorks). The DISC software was used for idealization (github.com/ChandaLab/DISC). Kinetic modeling was performed using QuB (qub.mandelics.com). All custom Matlab scripts are available from the corresponding authors upon reasonable request.

For manuscripts utilizing custom algorithms or software that are central to the research but not yet described in published literature, software must be made available to editors/reviewers. We strongly encourage code deposition in a community repository (e.g. GitHub). See the Nature Research guidelines for submitting code & software for further information.

Data

Policy information about availability of data

All manuscripts must include a data availability statement. This statement should provide the following information, where applicable:

- Accession codes, unique identifiers, or web links for publicly available datasets
- A list of figures that have associated raw data
- A description of any restrictions on data availability

Visualization in Fig. 1 included publically available PDB 20YG and PDB 6UQC. The data that support the findings of this study are available from the corresponding authors upon reasonable request.

| Field-spe | cific reporting | |
|--------------------------------------|--|--|
| Please select the or | ne below that is the best fit for your research. If you are not sure, read the appropriate sections before making your selection. | |
| ∑ Life sciences | Behavioural & social sciences Ecological, evolutionary & environmental sciences | |
| For a reference copy of t | he document with all sections, see <u>nature.com/documents/nr-reporting-summary-flat.pdf</u> | |
| | | |
| Life scier | nces study design | |
| All studies must dis | close on these points even when the disclosure is negative. | |
| Sample size | Statistical methods were not used to determine sample sizes. Electrophysiology experiments were performed on 5 replicates. Single molecule experiments provided >100 molecules per imaging condition. Each fcAMP concentration was recorded at least in duplicate on either a different ZMW array, chip and/or protein preparation to ensure consistent results. Experiments were repeated until s.e.m. values were sufficiently low for reliable dwell time analysis and comparisons between HCN1SM and HCN2SM. | |
| Data exclusions | Single-molecule time series were removed from analysis based on pre-established criteria. Traces were not included if: a given ROI featured more than 4 eGFP photobleaching steps (indicating more than molecule), the data was too noisy (SNR < 1.5) to reliable analysis, or if more than 5 ligand-bound states were identified. | |
| Replication | Data presented are an amalgam of different protein preparations (HCN1SM, n = 2; HCN2SM, n = 3) and collected across multiple ZMW chips (HCN1SM, n = 3, HCN2SM, n =4). All attempts provided consistent results. | |
| Randomization | The samples were not randomized as the experimental condition is systematic. | |
| Blinding | imentalists were not blinded to conditions or analysis as the procedure is systematic. Image processing and analysis were largely nated using predefined criteria described in the Methods of the manuscript. | |
| | g for specific materials, systems and methods on from authors about some types of materials, experimental systems and methods used in many studies. Here, indicate whether each material, | |
| | ed is relevant to your study. If you are not sure if a list item applies to your research, read the appropriate section before selecting a response. | |
| | perimental systems Methods | |
| n/a Involved in th | · _ _ · | |
| Eukaryotic | | |
| Palaeontology MRI-based neuroimaging | | |
| Animals and other organisms | | |
| Human research participants | | |
| Clinical dat | a | |
| Antibodies | | |
| Antibodies used | Alpaca anti-GFP VHH, biotinylated (GFP-TRAP) from Chromotek (gtb-250). Purchased GFP-TRAP was provided at 1 mg/mL (MW = 13.9 kDa) and diluted to 10 nM in TBS (300 mM NaCl, 20 mM Tris HCl, pH = 7.9) prior to use (1:7200 dilution). | |
| Validation | Specific binding of eGFP-tagged proteins to the glass or ZMW surface were tested in the presence and absence of GFP-TRAP (Extended Data Fig. 2). Chromotek reports a KD of 1 pM for GFP-TRAP/ GFP interaction and we did not notice any decay in the number of surface tethered molecules within a typical imaging session (1-2 hours). Full details on GFP-TRAP validation can be found at https://www.chromotek.com/products/detail/product-detail/gfp-vhh/ | |

Eukaryotic cell lines

| , , , , , , , , , , , , , , , , , , , | |
|--|--|
| Policy information about <u>cell lines</u> | |
| Cell line source(s) | Freestyle HEK293-F cell line obtained from Thermofisher Scientific (Cat #R79007) |
| Authentication | Cell line was not authenticated. |
| Mycoplasma contamination | Cells were not tested for cytoplasm contamination |
| | |